TECHNICKÁ UNIVERZITA V LIBERCI
Fakulta strojní

Investigation of the Cavitation Aggressiveness Using PVDF Sensors

Diplomová práce

Studijní program: N2301 – Mechanical Engineering
Studijní obor: 2302T010 – Machines and Equipment Design

Autor práce: **Myka Mae Campo Duran**
Vedoucí práce: Ing. Miloš Müller, Ph.D.

Liberec 2019

TECHNICAL UNIVERSITY OF LIBEREC
Faculty of Mechanical Engineering

Investigation of the Cavitation Aggressiveness Using PVDF Sensors

Master thesis

Study programme: N2301 – Mechanical Engineering
Study branch: 2302T010 – Machines and Equipment Design

Author: **Myka Mae Campo Duran**
Supervisor: Ing. Miloš Müller, Ph.D.

Liberec 2019

TECHNICAL UNIVERSITY OF LIBEREC
Faculty of Mechanical Engineering

Master Thesis Assignment Form

Investigation of the Cavitation Aggressiveness Using PVDF Sensors

Name and Surname:	**Myka Mae Campo Duran**
Identification Number:	S17000401
Study Programme:	N2301 Mechanical Engineering
Specialisation:	Machines and Equipment Design
Assigning Department:	Department of Power Engineering Equipment
Academic Year:	**2018/2019**

Rules for Elaboration:

1. State of art in the investigation of the cavitation aggressiveness.
2. Definition and preparation of the experimental setup.
3. Selection of an appropriate method for the bubble generation.
4. Preparation and testing of PVDF sensors for the measurement of the cavitation aggressiveness.
5. Realization of cavitation aggressiveness measurements using PVDF sensors.
6. Analysis of results and their interpretation regarding the pitting tests.

Scope of Graphic Work:	10 stran
Scope of Report:	50 stran
Thesis Form:	printed
Thesis Language:	English

List of Specialised Literature:

[1] KIM, Ki-Han, Georges CHAHINE, Jean-Pierre FRANC a Ayat KARIMI. *Advanced experimental and numerical techniques for cavitation erosion prediction*. Dordrecht: Springer, [2014]. Fluid mechanics and its applications, v. 106.

[2] *Acoustic cavitation and bubble dynamics*. New York, NY: Springer Berlin Heidelberg, 2017. ISBN 9783319682365.

[3] BRENNEN, Christopher E. *Cavitation and bubble dynamics*. New York: Oxford University Press, 1995. ISBN 0195094093.

[4] FRANC, Jean-Pierre a Jean-Marie MICHEL. *Fundamentals of cavitation*. Boston: Kluwer Academic Publishers, c2004. ISBN 1402022328.

Thesis Supervisor:	Ing. Miloš Müller, Ph.D. Department of Power Engineering Equipment
Date of Thesis Assignment:	1 November 2018
Date of Thesis Submission:	30 April 2020

Technická univerzita v Liberci
-8-

prof. Dr. Ing. Petr Lenfeld
Dean

doc. Ing. Václav Dvořák, Ph.D.
Head of Department

Liberec 1 February 2019

Declaration

I hereby certify I have been informed that my master thesis is fully governed by Act No. 121/2000 Coll., the Copyright Act, in particular Article 60 – School Work.

I acknowledge that the Technical University of Liberec (TUL) does not infringe my copyrights by using my master thesis for the TUL's internal purposes.

I am aware of my obligation to inform the TUL on having used or granted license to use the results of my master thesis; in such a case the TUL may require reimbursement of the costs incurred for creating the result up to their actual amount.

I have written my master thesis myself using the literature listed below and consulting it with my thesis supervisor and my tutor.

At the same time, I honestly declare that the texts of the printed version of my master thesis and of the electronic version uploaded into the IS STAG are identical.

3. 5. 2019

Myka Mae Campo Duran

ABSTRACT

The assessment of aggressiveness of cavitation phenomena through direct measurement of impact forces produced by bubble collapse is studied. This was done by recording impact forces from a commercially available Polyvinylidene Fluoride (PVDF) film sensor which is exposed to cavitation generated by ultrasonic transducer equipment. The ideal number of runs which will better represent the cavitation phenomena was first identified. Results showed good repeatability of every run and that a minimum of 3 experimental trials with time duration of 15 ms are enough to get a consistent data. The preparation of the PVDF films was optimized by selecting among four PVDF films that were setup differently, namely, a PVDF film as obtained from the supplier, a PVDF film topped with one layer of tape as an added protection, PVDF film with two layers of protective tape, and lastly a PVDF film which is folded into half. The PVDF film with one layer of tape is found to be the most suitable film for aggressiveness tests in terms of sensitivity and durability from cavitation damage. This film was then subjected to three different vibration amplitudes and it showed that increasing the oscillation amplitude leads to stronger impacts. Although most impacts were seen to occur at each horn vibration period, there were prominent high impact forces observed to arise after some cycles of horn vibration. This suggests that bubbles coagulate to form large cavity and then collapse more violently at a frequency lower than the frequency of ultrasonic horn vibration. Moreover, these strong impacts occur at a frequency that decreases as the vibration amplitude is increased. The obtained impact force signal was then compared to a previously obtained pitting test data which utilized the same experimental setup as used in this study. A remarkably high difference in the order of magnitude was seen between the cumulative peak rate and pit rate indicating that not all impacts cause pits on the surface of the material. Additionally, if it is assumed that a pit is formed from a single impact force during the incubation period, then a load of 319 N is necessary to create a 0.9 μm diameter pit on aluminum alloy.

ACKNOWLEDGEMENTS

I would like to express my deepest gratitude to my supervisor, Ing. Miloš Müller, Ph.D., whose expertise, huge support, and continuous guidance have greatly helped me with this thesis study. A big appreciation also goes to Ing. Jan Hujer who assisted me in the laboratory and advised me when I was analyzing my data. I would also like to thank Mr. Rush Salonga who was with me most of the time in the laboratory as we help each other in our respective experiments. I am also greatly indebted to Mr. Gafaru Moro who gave me a helping hand during my experiments and has proofread my write-up. I also wish to thank Ing. Edmund Ofei Aidoo for sharing with me his experimental data from his previous study and for giving me overflowing pieces of advice throughout this work. I will also be forever grateful to the Ministry of Education, Youth and Sports for granting me financial support in my master's study through the Czech Government Scholarship. This whole wonderful journey would have not been possible without this.

This thesis study was written as part of the project "Experimental, theoretical and numerical research in fluid mechanics and thermomechanics, no. 21291" with the support of the Specific University Research Grant, as provided by the Ministry of Education, Youth and Sports of the Czech Republic in the year 2019.

TABLE OF CONTENTS

NOMENCLATURE

List of Symbols

Roman Letters

Symbol	Description	Unit
a_c	Indentation contact radius	[m]
c	Speed of sound	[m/s]
c_l	Speed of sound of liquid	[m/s]
c_s	Speed of sound of solid wall	[m/s]
d_p	Pit diameter	[m]
E_s	Young's modulus of solid wall	[N/m ^{2}]
F_{max}	Maximum force	[N]
F_{mean}	Mean impact force	[N]
F	Peak impact force	[N]
F_0	Reference peak force	[N]
g	Acceleration due to gravity	[m/s^2]
h	Height	[m]
h_p	Pit depth	[m]
$\dot{n}$	Peak rate	[1/mm^2/s]
$\dot{n}_0$	Reference peak rate	[1/mm^2/s]
p	Pressure	[Pa]
p_{g0}	Pressure of the gas inside the bubble at initial state	[Pa]
p_v	Vapor pressure of the liquid	[Pa]
p_∞ (t)	Liquid pressure at an infinite distance from the bubble	[Pa]
p'	Instantaneous pressure generated on the solid surface	[Pa]
R	Bubble radius	[m]
$\dot{R}$	First order derivative of bubble radius with respect to time	[m/s]
$\ddot{R}$	Second order derivative of bubble radius with respect to time	[m/ s ^{2}]

R_0	Initial bubble radius	[m]
R_{ind}	Spherical indenter radius	[m]
S	Surface tension coefficient	[N/m]
t	Time	[s]
T_c	Critical point temperature	[K]
T_r	Triple point temperature	[K]
U_{max}	Maximum voltage	[V]
U	Peak impact voltage	[V]
U_0	Reference voltage	[V]
v	Velocity	[m/s]
v_j	Microjet velocity	[m/s]

Greek Letters

β	Coefficient of compressibility	[-]
ε	Strain	[-]
ε_l	Pitting strain	[-]
γ	Polytropic exponent of the gas	[-]
ρ_l	Density of the liquid	[kg/m^3]
ρ_s	Density of the solid wall	[kg/m^3]
τ	Rayleigh time	[s]
τ	Impact duration time (for drop ball calibration method)	[s]
μ	Dynamic viscosity	[Pa s]
φ	Velocity potential	[m^2/s]

List of Abbreviations

DAQ	Data acquisition system
PVDF	Polyvinylidene Fluoride
FFT	Fast Fourier Transform
MS/s	Megasamples per second

1 INTRODUCTION

The transformation of liquid to vapor through pressure reduction is known as the cavitation. This is visible as just small bubbles but implosion of these bubbles generates highly significant effects on many applications. Cavitation was actually first discovered due to its damaging effects in hydraulic machines. It is famously known on its destructive erosion effects on pumps, turbine blades and ship propellers leading to decrease in efficiency and eventually to its failure. However, there are also cases when cavitation becomes beneficial. It is widely used for medical applications such as shock wave lithotripsy and cancer therapy. This is also the same mechanism behind ultrasonic cleaning and it has also shown potential in treating wastewater. All these harmful and valuable effects have drawn many researchers to do more in depth study of cavitation. Yet, there is still an unestablished knowledge on precisely predicting the extent of cavitation damage. This information will lead to a development of a cavitation prediction tool that could substantially help decrease or avoid the unwanted deleterious effects brought by cavitation. This could also be a helpful tool to control cavitation aggressiveness and use it in a valuable way.

This thesis study aims to determine the aggressiveness of the cavitation by analyzing the forces from impacts of each bubble collapse and relate this to the pits formed on the material's surface. The bubbles studied here are in the form of cloud cavitation in order to model a more realistic scenario. This will be done through formation of cloud cavitation from strong acoustic waves.

2 REVIEW OF RELATED LITERATURE

This chapter provides the definition of cavitation and how an individual bubble evolves. This also indicates the effects of cavitation. To further understand what caused these effects, different impact loads during bubble collapse and how material responds to it are discussed. Research works on the different approaches to cavitation aggressiveness investigation were also reviewed.

2.1 Definition of Cavitation

Cavitation is defined as the breaking down of liquid medium leading to the formation of vapor cavities. The vapor cavities result from the growth of tiny void or nuclei formed during the inception of cavitation. The growth of nuclei is realized when the local pressure of the liquid drops below the vapor pressure forcing the liquid to form vapor cavities [1]. Figure 1 is a phase diagram that further explains this phenomenon from a classical thermodynamics point of view.

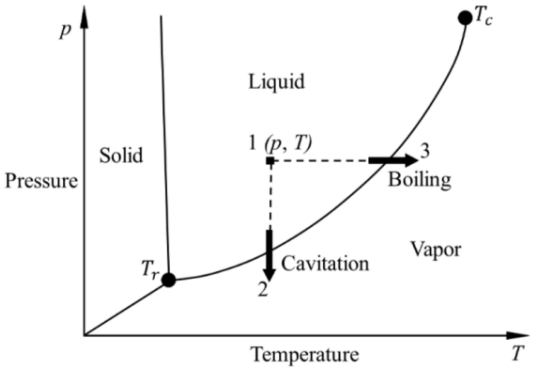

Figure 1. Phase diagram of water. T_r is the triple point and T_c is the critical point. [2]

Vaporization of liquid can be done in two different approaches. It can either be driven by temperature or pressure change. From Figure 1 above, increasing the temperature whiles maintaining a constant pressure is called boiling (point 1-3) whereas decreasing the pressure while having a constant temperature is known as cavitation (point 1-2). Process 1-2 is the only region of interest for cavitation studies [2][3][4].

Liquid holds a large amount of micron air bubbles or gas particles where cavitation can initiate. These are known as the cavitation nuclei and these serve as starting points of nuclei breakdown. These nuclei are either formed due to the creation of a new cavity or due to the expansion of a pre-existing one where macroscopic effects can be observed. When these nuclei are formed due to macroscopic fluctuation or molecular interaction, this is known as *homogenous nucleation*. Moreover, nucleation sites can also be found as trapped gases on available suspended micron solid particles in the liquid and discontinuities of solid surfaces. When nuclei arise from these sites, it is called *heterogeneous nucleation*. In cases where a liquid has no nuclei, a very large amount of tension (in the order of tens of MPa) is necessary to break the liquid cavity into molecule [3].

2.2 Types of Cavitation

Cavities are formed from the creation of void and filling this void with vapor until it becomes saturated [2]. In reality, cavitation bubbles can be composed of gas, vapor or a mixture of both. In a bubble containing gas, its growth can be due to pressure reduction or increase in temperature. This is called as *gaseous cavitation*. Gas-filled bubble can also be formed by so-called *degassing* which is done through diffusion as gas comes out of the liquid. On the other hand, a vapor-filled bubble is formed by pressure reduction at constant temperature. This is known as *vapor cavitation*. Another way of creating vapor-filled bubble is through *boiling* using enough rise in temperature, as discussed previously. In the real situations, the bubble is considered to be a mixture of gas and vapor with one being more dominant [1].

The inception of cavitation can be of different forms. The rapid growth of small air nuclei in low pressure areas produces the *transient isolated bubbles*. These move along the flow and subsequently collapse in high pressure region. The *attached or sheet cavities* can be seen on the leading edge of a body such as the blades and foils. These occur when a cavity is attached to rigid boundary of an immersed body and remains fixed in position in an unsteady state. *Cavitating vortices*, on the other hand, are evident on turbulent wakes, propeller blade tips and other regions with high shear where there is low-pressure core of vortices [4].

There are a lot of ways through which cavitation can happen. The *hydrodynamic cavitation* happens when there is a pressure reduction of flowing liquid due to the geometry of the system such as pump or propeller where acceleration of flow occurs. Cavitation can also commence on a liquid at static state when it is applied with strong acoustic field having sufficiently low pressure enough to break down the liquid to form bubbles which grow during the rarefractional half cycles of the acoustic wave [5]. This is known as *acoustic cavitation*. Another way of generating bubbles is through *optical cavitation* where photons of high intensity laser light are directed on the liquid, rupturing it and creating the bubbles. This is specifically known as *laser-induced cavitation.* Other method of bubble formation is through the use of charged particle which when sent through the liquid forms an ionization trail. These ions transmit energy to electrons which gives up to around 1000 electron volts of energy in a small volume causing rapid local heating. This process is called *particle cavitation* and is based on growth of bubbles in liquid by superheating (boiling). Overall, the hydrodynamic and acoustic cavitation are both due to pressure reduction enough to break tension in the liquid while optic and particle cavitation are a result of local deposition of energy [1].

In this study, acoustic cavitation formed from ultrasonic waves will be considered.

2.3 Effects of Cavitation

When bubbles collapse next to an adjacent boundary, there will be pitting or erosion on the surface. This can either be viewed to create beneficial or detrimental effects depending on the application. For instance, ultrasonic cavitation is widely known for its cleaning applications wherein the implosion of cavitation bubbles aids in the removal of contaminants in the surface submerged in an ultrasonically activated liquid without creating damage on the surface itself [6]. Cavitation shotless peeing is also gaining attention as a process in improving surface material property. It is proven to enhance hardness and introduce residual stress in the material by 61% and 148%, respectively for aluminum alloy [7]. This increase of the compressive residual stress on the metallic material was also observed experimentally by Odhiambo et. al. [8] and regarded this is as the key factor to enhancing the material's fatigue life. They found that the fatigue strength of the cavitation peened material is superior than the non-penned and shot-peened material by 79 and 27

MPa, respectively. Additionally, Gao et. al. [9] found that cavitation peening can improve the surface hardness of a stainless steel and nickel alloy without increasing its surface roughness.

Formation of bubbles due to cavitation phenomena hold promising applications in different fields. It is beneficial in the field of medicine where it brings advantageous result for specific surgical and medical procedures such as emulsifying tissue in cataract patients, reducing kidney and gall stones in shock wave lithotripsy procedures, manipulating DNA in individual cells, creating minute incisions, or targeting cancer cells [10]. Cavitation may also be applied in waste water treatment. The formation of high temperature and high pressure environment with high speed microjet from hydrodynamic cavitation cause the subsequent creation of highly reactive free radicals from water which are needed for degradation reactions [11]. Furthermore, it has also proven to be effective in the treatment of wastewater containing organic pollutants such as pesticides, pharmaceuticals, dyes, phenolic compounds and industrial effluents [12]. Cavitation can also be applied in the food industry such as modification of milk components in dairy products and improving food safety by destroying spoilage and pathogenic microorganisms [13].

The favorable effects of cavitation were discovered only recently with the on-going advancement of knowledge on cavitation phenomena. In reality, cavitation was first known due to its adverse effects. Actual cavitation was first studied by Barnaby and Parsons in 1893 due to a propeller failure in a British high-speed warship which was said to be instigated by the formation of bubbles on the blades. Parsons then did a follow up study in 1895 by creating the first water tunnel which then led to the discovery of cavitation and its damaging effect on the propeller. Since then several studies commenced to study this damaging effects. [14] [15]

Cavitation bubble collapse near a solid wall causes highly localized, large amplitude shockwaves and microjets which consequently generates intense surface stresses at the point of collapse. Destructive shock waves knock out the material leaving it with pits that can grow larger with continuous cavitation. When this is done repeatedly, it causes fatigue failure eventually leading to total material damage [16]. It deteriorates performance of hydraulic equipment, causes noise, mechanical vibration. This is the reason why cavitation is considered a huge problem when it comes to hydraulic machinery in marine and automotive industry where turbine, pump and ship propellers are present [14]. Moreover, it also affects energy plants such as nuclear reactors where

cavitation is visible in reactor pump's impeller blades and in places with high velocities such as impeller outlet and diffuser [17].

Figure 2. Cavitation erosion on pump impeller [17]

Cavitation damage is also found as an alarming phenomenon when present in human body. Trauma in brain after an impact leads to the formation of cavitation and it is claimed to be the damaging mechanism behind this traumatic injury [18]. Cavitation erosion is also evident on the surface of implanted mechanical heart valves causing its fractures. The cavitation is induced during the closing of the valve during which a low pressure region is developed by the squeeze flow [19].

2.4 Dynamics of the Cavitation Bubble

2.4.1 Spherical Bubble

Cavitation bubbles can be modeled as either spherical or non-spherical. For spherical bubbles, several studies were done to develop a model to illustrate the different cases of bubble behavior such as bubble growth from nucleus, bubble collapse, and bubble oscillations. Besant in 1859 was the first to study the liquid motion induced by a spherical cavity in an infinite medium under constant pressure at infinity. Later on, Rayleigh in 1917 solved this for cases of inviscid liquid. This was then improved by Plesset in 1954 to include cases for viscous and non-compressible liquid [4].

To completely analyze bubble dynamics, it is necessary to incorporate balance of mass, momentum, energy and entropy in space and time. To reduce this problem, a simplification can be applied. Important assumptions include that: the bubble remains always spherical, the bubble center is stationary and fixed in space, bubble is an infinite body of liquid, bubble content is homogeneous, liquid is incompressible and either Newtonian or inviscid, and the gravity acting on the bubble is neglected. Furthermore, no heat and mass transfer is considered. Also, the gas content of the bubble is constant and there is no heat exchange with the environment, and the bubble is considered as saturated with vapor whose partial pressure is the same as the vapor pressure of the bulk liquid [4] [20]. With all these simplifications, the time evolution of bubble radius was derived and is known as the *Rayleigh-Plesset equation*:

$$\rho\left[R\ddot{R} + \frac{3}{2}\dot{R}^2\right] = p_v - p_\infty(t) + p_{g0}\left(\frac{R_o}{R}\right)^{3\gamma} - \frac{2S}{R} - 4\mu\frac{\dot{R}}{R} \quad (1)$$

where ρ is density, μ is dynamic viscosity, S is surface tension, $p_\infty(t)$ is pressure far from the bubble at time t, p_v is the pressure of vapor inside the bubble, p_{g0} is the pressure of gas inside the bubble at initial state, γ is the polytropic exponent of the gas, R is the bubble radius at time t, R_o is the initial bubble radius, $\dot{R}$ and $\ddot{R}$ are the first and second order derivatives of bubble radius with respect to time.

This equation allows the determination of the growth of the bubble radius and the pressure field in the liquid when the law $p_\infty(t)$ is known. This equation is highly non-linear due to the inertial terms and often can only be solved using numerical calculation [4].

From this equation, four factors are seen to be affecting spherical bubble dynamics. The first one is the pressure effect from the term $p_v - p_\infty(t)$. This difference of applied pressure to the vapor pressure is the most important factor because evolution of the bubble essentially relies on it. The next factors consider the effect from non-condensable gas, surface tension and surface viscosity [21].

If the liquid is inviscid and the effects of non-condensable gas and surface tension are negligible, then it will give us a simpler equation known as the *Rayleigh equation* shown below. This happens when the bubble is much bigger than the original nucleus.

$$\rho\left[R\ddot{R} + \frac{3}{2}\dot{R}^2\right] = p_v - p_\infty(t) \tag{2}$$

Integrating this equation given that the applied pressure p_∞ is constant, we can get

$$\dot{R}^2 = \frac{2}{3}\frac{p_v - p_\infty}{\rho}\left[1 - \left(\frac{R_0}{R}\right)^3\right] \tag{3}$$

If p_∞ is less than p_v, the bubble will grow such that R will be greater than R_0. The rate of bubble growth can then be approximated as

$$\dot{R} \cong \sqrt{\frac{2}{3}\frac{p_v - p_\infty}{\rho}} \tag{4}$$

However, if p_∞ is greater than p_v, the bubble size decreases. This is what happens during bubble collapse process. Assuming that the effects of viscosity, non-condensable gas and surface tension are still negligible, rate of decrease of bubble size is

$$\dot{R} \cong -\sqrt{\frac{2}{3}\frac{p_\infty - p_v}{\rho}\left[\left(\frac{R_0}{R}\right)^3 - 1\right]} \tag{5}$$

During bubble collapse, the radius goes to zero and by numerically integrating this equation we can obtain the bubble collapse in a characteristic collapse time τ called the Rayleigh time which is

$$\tau \cong 0.915\, R_0\sqrt{\frac{\rho}{p_\infty - p_v}} \tag{6}$$

This is the time for the bubble to fully disappear [21].

2.4.2 Non-Spherical Bubble

The assumptions made during spherical bubble behavior analysis are not practical. For real cases, factors such as gravity, pressure gradients, and flow turbulence have non-uniform pressure distribution which then cause the deformation of the bubble's spherical shape.

Plesset and Chapman in 1971 calculated the time evolution of deformation of the bubble interface. They used numerical simulation wherein a spherical bubble is bound to collapse under constant pressure difference. It is assumed that the surface tension, viscosity and liquid compressibility are negligible and that bubble only contains vapor at vapor pressure. Since it is incompressible, the velocity potential φ can be calculated from Laplace equation $\Delta\varphi = 0$ with appropriate boundary conditions at the bubble interface, the solid wall and in the free liquid. The velocity of the bubble interface can be computed using the equation $v_i = d\phi / dx_i$. Using generalized Bernoulli equation, the following can be deduced [4]:

$$\frac{d\varphi}{dt} = \frac{\partial\varphi}{\partial t} + v_i \frac{\partial\varphi}{\partial x_i} = \frac{p_\infty - p_v}{\rho} + \frac{v^2}{2} \tag{7}$$

The time evolution of bubble can be determined by calculating this equation in a series of boundary conditions at time t + dt.

The evolution of bubble interface close to a wall can then be illustrated as shown in Figure 3.

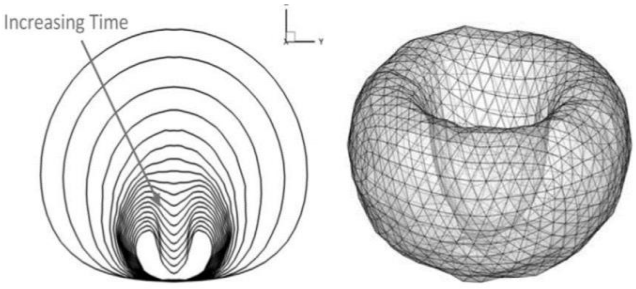

Figure 3. Deformation of bubble interface as calculated by Plesset and Chapman [22]

As observed in Figure 3, the interface near the wall flattens through time and at the same time a hollow is formed on the other side. The re-entrant jet which develops from this hollow region is directed to the solid wall. This pierces the bubble and hits the wall at a very high velocity causing pits. Cumulative effects of this lead to what is known as cavitation erosion [4].

2.5 Cavitation Impact Loads at Collapse near a Solid Wall

The bubble collapse is due to compression when exposed to high pressure. The compression could be so intense that collapse goes violently. These collapses are accompanied by high velocity micro-jets and strong shock waves [2].

When the bubble grows, the radial flow of the liquid is hindered by the nearby wall. This causes pressure gradient wherein the pressure at the area close to the wall is low while the liquid pressure far from the wall is high. Hence, bubble collapse starts when the liquid at the bubble interface farthest from the solid wall begins to focus and form micro-jet which then accelerates towards the bubble interface close to the solid wall. Experimental works by Philipp and Lauterborn showed that the pressure gradient along the wall leads to varying accelerations depending on the location of the bubble interface with respect to the solid wall. Regardless of the bubble distance, it showed that all bubbles are being directed towards the solid wall. Kornfeld & Suvorov was the first to introduce the idea of micro-jet directing to the solid wall and this was observed experimentally by several studies [2].

The micro-jet velocity, v_j, is estimated to reach few hundreds of m/s. However, the impact velocity of this micro-jet is slowed down by the layer of water present in between the bubble and the solid wall. With an increase of the water layer thickness, the impact intensity decreases [2].

The actual impact pressure from the micro jet towards the solid wall can be estimated using the water-hammer phenomenon and conservation of mass and momentum as [2]

$$p = \frac{\rho_l c_l v_j}{1 + \frac{\rho_l c_l}{\rho_s c_s}} \tag{8}$$

where ρ is density and c is the speed of sound. The subscript l and s indicates if the parameter is for liquid or for the solid wall. Assuming that the solid wall is a perfectly rigid body, its Young's modulus will go to infinity. Knowing that the formula of the speed of sound is

$$c_s = \sqrt{\frac{E_s}{\rho_s}} \tag{9}$$

therefore, the value c_s will also be infinite. The impact pressure will then be simply

$$p = \rho c v_j \tag{10}$$

where c is the speed of sound. Typical value for the pressure increase in the case of water is 150 MPa which is not far from the value obtained for shock wave. Both the shock wave and the microjet produces high pressure pulses which can reach the yield strength of common metals [4].

The impact pressure value increases with bubble size [4]. Rayleigh developed an equation to estimate the pressure from collapse of a sphere bubble with radius R when the micro jet hits the wall as follows [17]:

$$\frac{p'^2}{2\beta} = \frac{1}{2}\rho\dot{R}^2 = \frac{p_\infty}{3}\left[\left(\frac{R_0}{R}\right)^3 - 1\right] \tag{11}$$

where P' is the instantaneous pressure generated on the solid surface, β is the coefficient of compressibility. Impact from microjet is regarded in studies as the main cause damage [17].

As the micro-jet pierces the bubble interface before it hits the solid wall, a shock wave called jet shock wave is generated. Another shock wave comes as soon as the bubble collapses and this is called the collapse shock wave which happens due to high compression of the gas bubble inside. These two successive shock waves were observed experimentally by Philipp and Lauterborn and found out that intensity of the shock waves goes weak as the bubble becomes more asymmetric. This happens when reducing the bubble stand-off distance (γ), which is the ratio of initial bubble distance from the solid wall to the maximum bubble radius [2].

After the initial collapse, the bubble forms a vapor torus. This torus divides into several smaller bubbles which also collapse subsequently. This collective cloud collapse creates additional impact towards the solid surface. The pressure wave produced from this increase the collapse velocity of the neighboring bubbles which then leads to the increase of their pressure wave amplitudes [4].

Following the impact of a jet, a toroidal cavity is formed close to the wall. This acts a force on the wall causing what is called as the splash effect. In a study conducted by Tong et.al, [23] they found out that for a certain interval of stand-off distance, this splash effect produces higher hydrodynamic pressure on the solid wall than that of the micro-jet.

In case of acoustic cavitation, collective collapse can happen which is the collapse of a cloud of bubbles. The rapid oscillation in the liquid forms many bubbles that collapse together near the solid wall. The resulting collective impact can be more violent than individual collapses [4].

2.6 Material Response to Cavitation

Cavitation erosion does not only depend on the hydrodynamic mechanism impacts but also on the mechanical properties of the material. This includes tensile strength, resilience, ductility, hardness, fatigue resistance and microstructure [24][25]. Thus different materials respond differently to cavitation effects. Until now, there is still no established data on predicting the extent of cavitation damage based on material property. However, the relationship of the two can be further understood using erosion curve shown in Figure 4.

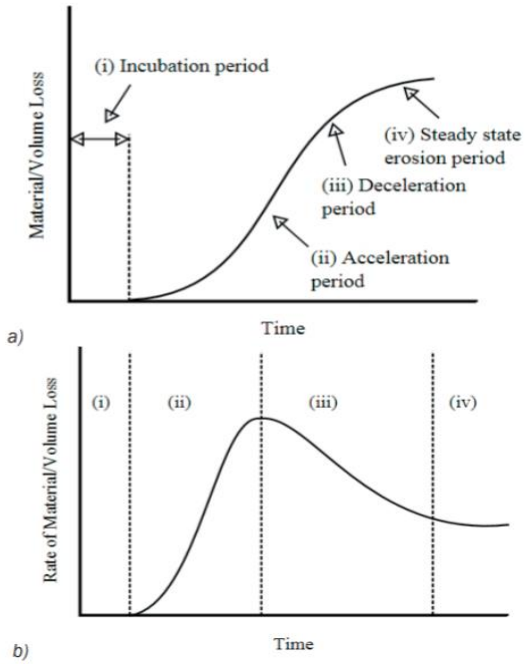

Figure 4. Material loss through time [24]

The generalized S-shaped erosion curve of mass loss vs. time in Figure 4 shows that the cavitation erosion is dependent on the duration of exposure. The shape of the curve can be different depending on the material property, e.g. if it is brittle or ductile.

There are four time phases of mass loss observed in cavitation erosion, namely: incubation period, acceleration period, deceleration period and steady state-period. During the incubation period, the material experiences high impact loads with magnitude exceeding the elastic limit of the material thus forming pits. The formation of these pits is called cavitation pitting. With the high impact stress ranging to a few GPa [2] from the bubble collapse, the material undergoes plastic deformation in the form of these pits but with no mass loss. Pits formed here are typically in the range of a few microns to a few hundreds of microns in diameter [3]. Due to repetitive loading, fatigue is induced and internal stresses are accumulated under the surface. Continuous impacts on the solid wall leads to strain accumulation and development of work hardening specially in ductile materials. Subsequently, micro-cracks will appear around the grain boundaries and surface heterogeneities and will eventually propagate outwards. The material will not be able to endure the impacts and it will break causing mass loss. Repetitive impacts from bubble collapses leads to cavitation erosion. This commences the transition from incubation to the acceleration period. Following the acceleration period is a decrease in the mass loss rate, called the deceleration period, then it will reach a steady state with an almost constant mass loss rate. In this case, the surface that was strongly fractured now behaves as a protective cushion [24].

2.7 Cavitation Aggressiveness Investigation Approaches

Several researchers have investigated on the intensity of cavitation and so far, these experimental approaches can be classified into two: through conduction of pitting test and by directly measuring the impact loads hitting the wall.

2.7.1 Cavitation Pitting Test

Pitting test is conducted by measuring the pits which are seen on the wall of the material exposed to cavitation. The material is treated here as the virtual transducer. Theoretically, the material will only deform when yield stress in reached, therefore the threshold for pitting test is its yield stress. This approach is only appropriate when the cavitation is at the incubation period because the pits here are not overlapping [4]. This kind of test has been widely used by several researchers [3][5][26]. In a pitting test by Aidoo [27] on aluminum alloy exposed to ultrasonic cavitation, he

was able to get the cumulative pitting rate for different exposure time duration and the results demonstrate that the number of pits increases when exposure time is lengthened but the generation of larger pit volumes decreases as pitting rate increases. This indicates that the material could be experiencing work hardening. This is the mechanism behind strengthening of material by cavitation shotless peening.

Franc et. al. [26] studied cavitation erosion by conducting pitting test on aluminum alloy, nickel aluminum bronze alloy and duplex stainless steel. Cavitation tunnel was employed as the source of cavitation. Pits were assessed using contact profilometer. Pit counts and its geometry such as depth, surface area and volume were measured. Cumulative pitting rate in a logarithmic scale was also plotted vs the pit diameter. Same as Aidoo's cumulative pit graph, their results showed a linear curve in the logarithmic scale graph which denotes an exponential distribution relation between pitting rate and pit diameter. Moreover, they also concluded that the cavitation damage is not easily correlated to the material property, most specifically the elastic limit. The high strain introduced by cavitation impacts may have a great influence on the results and it is then recommended to include this factor in the analysis and not just solely base pitting results from the yield strength of the material.

Early studies of Berchiche et. al.[28] used pitting test to determine flow aggressiveness impacted on a 316L ductile stainless steel. Impact loads were derived from the pitting test results and the material properties. From this, an analytical model was established for the prediction of cavitation erosion in ductile materials. This model, however, ignored the influence of strain rate and it is only one-dimensional model.

2.7.2 Measuring Impact Loads

2.7.2.1 Nanoindentation Test

The impact load of the pits can be deduced from the pit's geometry and material property through nano-indentation test. In a study by Tzanakis et. al. [5], they used pitting test in characterizing cavitation aggressiveness on a steel sample subjected to ultrasonic cavitation. The hydrodynamic impact pressure was evaluated using reverse engineering involving analytical calculation based

from the pits' geometry. Similar concept was utilized by Carnelli et. al. [29] in their study for evaluation hydrodynamic impact pressure from hydrodynamic tunnel. Two tests were done, namely, pitting test and the nanoindentation test. The analysis was carried out by comparing the results between two tests. The idea is to adapt the concept from contact mechanics to determine the stress from the strain produced from a controlled nanoindentation test. The spherical indentation from the nanoindentation test introduces equivalent true strain (ε) which is empirically expressed by Tabor as

$$\varepsilon = 0.2\ \frac{a_c}{R_{ind}} \tag{12}$$

where a_c is the indentation contact radius and R_{ind} is the radius of the spherical indenter.

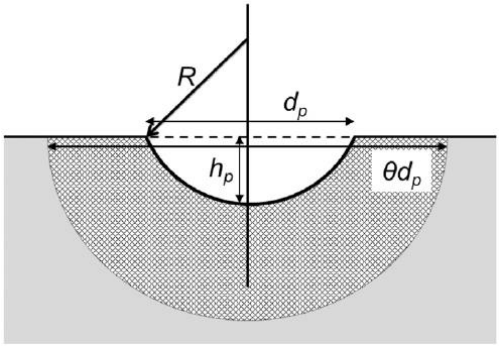

Figure 5. Schematic model of cavitation pit geometry. [29]

Based from Figure 5, d_p and h_p are the pit diameter and depth, respectively. From this illustration, it follows that $a_c = d_p/2$. The radius of the indenter can be expressed in relation with pit depth and diameter as

$$R_{ind} = \frac{\left(\frac{d_p}{2}\right)^2 + \left(h_p\right)^2}{2h_p} \tag{13}$$

Equation 12 can then be further expressed as

$$\varepsilon = 0.2\,\frac{d_p h_p}{\left(\frac{d_p}{2}\right)^2 + \left(h_p\right)^2} \tag{14}$$

Assuming that the pit depth us much smaller than the pit diameter, equation 14 can be simplified as

$$\varepsilon = \varepsilon_p \cong 0.8\,\frac{h_p}{d_p} \tag{15}$$

wherein this strain is also the same as ε_p which is the pitting strain. Through contact mechanics of materials, this calculated pitting strain can be used to determine the impact stress causing the pit.

The nanoindentation approach however pose a drawback. The indentation of spherical ball in reality can only be performed at a very low strain rate of 0.05 s^{-1} compared to the actual strain rate in the order of 10^3 s^{-1} produced by impacts from bubble collapse [29]. This high stain rate makes the reverse engineering process difficult and is also a concern raised by other researchers [26]. Though strain rate effect was taken into consideration in Carnelli's study through an empirical model and theoretical analysis, there is still a doubt of the accuracy of this reverse engineering method. In a study by Choi et. al.[22], they concluded that the use of Tabor equation can only accurately give the maximum effective stress experienced by the material and not the imposed load. The analogy derived through Tabor's equation largely underestimates this load.

2.7.2.2 Direct Impact Load Measurement

The pitting test is not capable of giving the actual value of the normal stress that has caused the pits. Instead, only a comparison with the yield strength can be made together with assessing its pit's geometry as discussed in nanoindentation test. To get a better characterization of cavitation aggressiveness, it is then important to measure directly the impact loads and compare it with the results from the pitting test. The bubble collapses occur very quickly, hence directly measuring the impact pressures requires a transducer with high natural frequency. Direct measurement approach was done by several researchers [30][31][32][33] including Franc et. al. [34] who specifically studied erosion generated from a high-speed cavitation loop. Bubble impacts were recorded using

a piezoelectric pressure sensor which expresses the signal in terms of voltage. From the impact signal, a cumulative peak rate vs. voltage amplitude was plotted and an exponential relationship was clearly observed. The comparison made between pitting rate and peak rate was found not simple because peak rate is dependent on the load threshold and the pitting rate depends on the set pit diameter threshold. These established thresholds are only based on prediction that values below these will not cause any pits. Different threshold values were considered in the study to make peak rates and pitting rates comparable in orders of its magnitude. They recommended to use a high level of load threshold in the analysis of peak rate to make the data comparable. This was the method used as a basis in setting the minimum threshold value. Through this, only high impact collapses will be considered and weak impacts that could not create pits on the material will be ignored. It was concluded though that there is still an uncertainty on the absolute values of the impact loads as these do not coincide with the data obtained from analytical examination of pits using nanoindentation test at low strain rate.

There is one major concern when using direct measurement approach for cavitation aggressiveness analysis. In reality, the sensitive area of the transducer (in range of millimeter) is much larger than the pressure impact (in the order of micrometers). This difference makes it difficult to accurately determine the pressure. To avoid the problem due to this difference in area between the sensor and the pressure impact, the force can be alternatively measured instead of pressure [4]. This is a problem acknowledged by several researchers [33] [35] setting this as a limitation in their studies.

2.8 Laboratory Testing Methods

Cavitation erosion depends not only on the material properties but also on the way cavitation is generated, whether by acoustic, hydrodynamic and laser light. This makes predicting the cavitation erosion difficult. The following subsections details the different ways of creating cavitation in a controlled environment for the purpose of research study, and how cavitation impacts are quantified.

2.8.1 Cavitation Equipment

Several laboratory techniques can be used to generate and study the dynamics of cavitation. A commonly used cavitation instrument used is the ultrasonic transducer. It provides cavitation by the introduction of strong acoustic waves. The continuous cyclic compression and tension forces in the liquid create cavities or voids. These develop into bubbles which can be classified as either stable or transient [24]. The stable bubbles can oscillate for several cycles but the transient bubbles grow up to less than one compression half-cycle and implodes. The ultrasonic cavitation instrument consists of a sonotrode tip or a horn that vibrates generating high frequency waves which form ultrasonic cavitation. It is a common instrument utilized by researchers in examining cavitation erosion resistance of materials. It is used by Tzanakis et. al. [36] in their study to determine the best possible steel materials for fluid machinery equipment which is known to be prone to cavitation erosion damage. Likewise, it is also used by Liu et. al.[37] and Pola [38] et.al. for cavitation erosion test on copper alloy and aluminum alloy, respectively.

Analysis of ultrasonic horn cavitation impacts was done by Vohra et. al. [35] by varying different parameters in the ultrasonic transducer setup to identify the effects of ultrasonic horn vibrating amplitude, stand-off distance and horn insertion depth. An ultrasonic horn with 12.8mm tip diameter was used and it is set to vibrate at a frequency of 20 kHz. The schematic diagram of their experimental setup is illustrated in Figure 6.

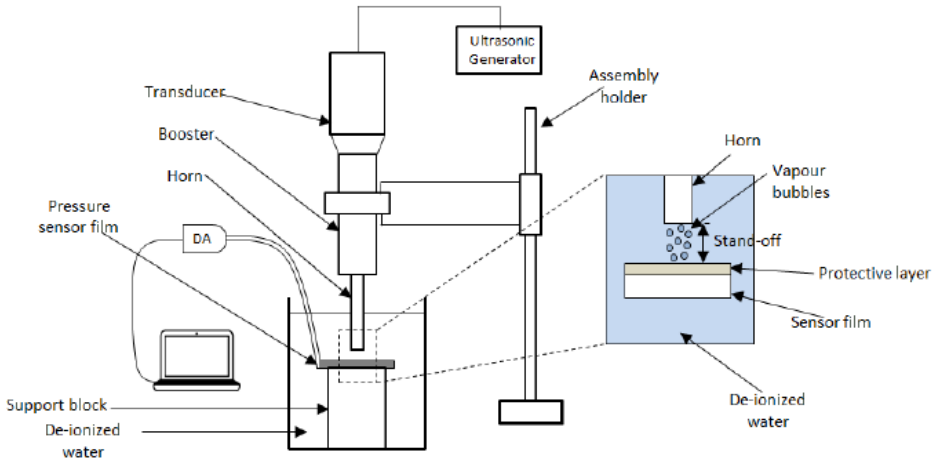

Figure 6. Experimental setup by Vohra et. al. on their study on ultrasonic horn cavitation [35]

To understand the effect of ultrasonic vibrating amplitude, the tip of the horn was set at a stand-off distance of 1mm from the sensor. It was found out that the increase of the amplitude leads to an increase in the collapse pressure and force. The large negative vibration cycle aids in the growth of cavities which will agglomerate resulting to a higher collapse impact pressure. The results of the observed variation in the force magnitude signal from different vibration amplitudes is regarded as an easy way to identify ultrasonic system suitable for different applications depending on the needed cavitation impact intensity. A lower ultrasonic vibration amplitude generating a lower force on the impacted material can be utilized for ultrasonic cleaning applications whereas higher vibration amplitude can be employed for metal and non-metallic surface treatment. Another parameter that was varied in their study is the stand-off distance. It was observed that increasing the stand-off distance while keeping the insertion depth of the horn fixed results to a decrease in the recorded pressure impacts. This result coincides with the observations of Paepenmöller et. al. [39] due to attenuation of the acoustic waves. Also, the increase of the static pressure at a larger stand-off distance causes cavitation bubble to collapse early when the surrounding pressure is higher than the vapor pressure therefore imparting lower pressure impacts. Same results were observed when the horn insertion depth was increased. At a deeper position of the horn relative to the liquid surface, the further growth of the bubble is impeded by the increase of the static pressure.

A cavitating jet can also be used to generate cavitation. This method is called cavitating jet method or Lichtarowicz cell. A jet is produced by a positive displacement pump that sends constant rate of liquid through a nozzle. Cavitation will start at the point where the diameter of the stream is the least. Bubbles will collapse towards the specimen situated along the path of the jet and at a certain distance below the nozzle.

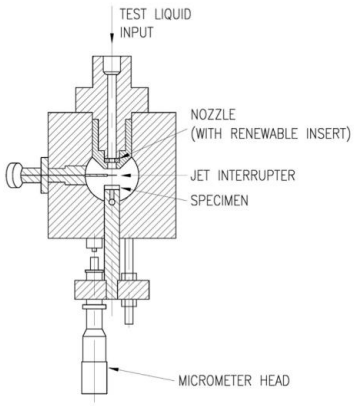

Figure 7. Cavitating jet equipment [17]

Another cavitating instrument that can be used is a water tunnel where cavitation is produced in the location where there is hydrodynamic pressure reduction. Cavitation is generated by using cavitators such as cylindrical bolt in the test section. Figure 8 shows the schematic diagram.

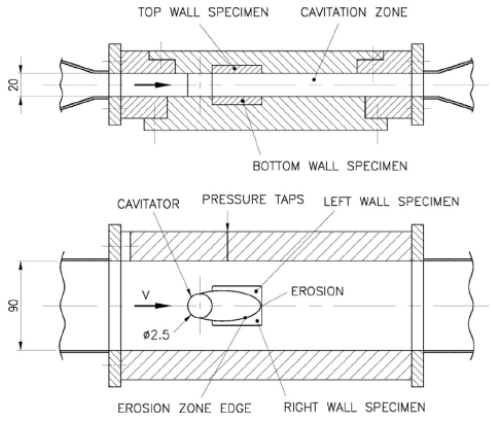

Figure 8. Test setup of cavitation water tunnel [17]

Alternatively, a venturi device can also be used which forms cavitation by restricting the fluid flow in the cross section thus reducing its pressure head and converting it to velocity head. This pressure reduction causes cavitation bubbles that collapse at the downstream of the throat.

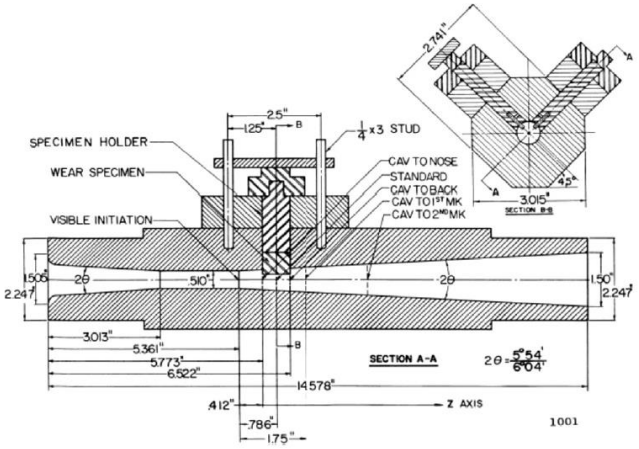

Figure 9. Venturi cavitation device[17]

There are more ways of producing cavitation in the liquid such as rotating disk device, rotating wheel, and cavitation chamber with slot cavitator. The choice of the simulation cavitation erosion method mostly depends on the specific application. For example, the use of vibratory equipment would not be suitable for erosion study for flowing system, instead, a venture device model must be used. The rotating disk device simulates well what is happening in turbomachine and this must be employed if that is the subject of interest [17].

In this study, vibratory equipment was chosen as the method for bubble generation because of its advantages: it is simple and easy to use; it requires only low inventory of the liquid; testing is quick because of the generated intensive cavitation; it is small and very economical; and results of the tests are repeatable [17] [40]. Note however, that this equipment forms different type of cavitation than what can be observed in hydraulic systems such as pumps and turbines [40].

2.8.2 Transducers Used

A popular sensor used in directly measuring cavitation impacts is a piezoelectric film called Polyvinylidene Fluoride (PVDF) film. It is a sensor which is capable of converting mechanical energy into electrical energy. In the case of cavitation, electrical signals are produced when cavitation bubble impacts strike the sensor. Conversion of the amplitude of the electrical signals into a corresponding force load can be done to analyze the intensity of the cavitation bubble collapse. This is the sensor preferred by many researchers [31] [33][39] because of its high

sensitivity to stress and strain and quick response time of approximately 100 ns [25]. In a study by Wang et. al.[33], they found that the 28 μm PVDF film they were using had a fast rising time of 56 ns and a sensitive bandwidth of about 10 MHz which they deemed to properly meet the needs for the purpose of cavitation impulsive impact analysis. Aside from that, it is convenient to use, because it can be easily fixed to wide variety of surfaces using simple adhesive. It does not need external power or complex circuitry to generate electrical signal. Moreover, the thin film's flexibility and smoothness avoids disturbance to the surface and the flow field. Also, it is a stable material which is resistant to water and chemicals [25].

Another sensor that can be used for the analyses of cavitation phenomena is needle-type hydrophone. This sensor is fabricated from PVDF film wherein one side of the PVDF film is attached to the end of the solid rod and the other end is exposed to acoustic waves [41]. It is a measuring instrument wherein bubble-induced pressure pulses are measured indirectly. During cavitation bubble collapse, the emitted acoustic transients are detected by hydrophone which is situated at a distance far away from the center of bubble collapse. It can be used for identifying the actual collapse pressure in a spherical bubble because the sound emission here contributes to the main part of the total collapse energy. However, it does not simply apply to non-spherical bubble collapses [33]. Hence, direct measurement of collapse impacts using PVDF film is a necessity. The needle type hydrophone sensor is mainly used by researchers to identify the pressure from far field during cavitation [42][43].

The PVDF sensor, in general, is a more suitable transducer for cavitation studies over other piezoelectric materials such as piezoelectric ceramic because the acoustic impedance of polymer is closer to water. Therefore, wave signal transmission from water to this kind of sensor is more efficient [41].

3 METHODOLOGY

The experimental design of this study is focused on the investigation of bubble collapses from cloud cavitation produced from ultrasonic waves. This chapter details the experimental setup including the cavitation equipment, the preparation of sensors used and its calibration. This also includes the post-processing of electrical signals from PVDF film sensor for further analysis.

3.1 Equipment Used

3.1.1 Vibratory Cavitation Erosion Equipment

A modified ASTM G32 vibratory equipment which is an ultrasonic device (UIP1000hdT - Hielscher) is utilized in this study. The equipment is composed of an ultrasonic transducer which is attached to a horn (BS2d22 - Hielscher) having 22mm diameter. This ultrasonic horn is vibrating at a frequency of 20 ± 0.2 kHz with amplitude of 57 μm which can be adjusted from 50 to 100%.

3.1.2 Sensors

3.1.2.1 PVDF Film

Preparation

A commercially available PVDF film (DTI-028K/L – Measurement Specialties, Inc.) was chosen as the sensor to measure the impact forces from the bubble collapses. This film has length of 30 mm and width of 12 mm. The piezo film has thickness of 28 μm and is sandwiched with protective coating on both sides giving it a total thickness of 40 μm. It has a capacitance of 1.38 nF. The film is fixed to a metal plate using a cyanoacrylate glue (Loctite Super Attack Power Flex Gel). The rivets of the sensor are fully covered with an epoxy glue isolating it from the metal plate to avoid disturbance of electrical signals. The fully prepared sensor is shown on Figure 10. The leads of the film are connected directly to the Data Acquisition System (DAQ) device (NI PXI-5105 12-Bit Digitizer – National Instruments) capable of reading signals at a maximum sampling frequency of 60 MS/s.

In this study, four PVDF configurations were utilized. The first configuration is the PVDF film as obtained from the supplier. The second is a PVDF topped with a single layer of transparent adhesive scotch tape (Manutape) which acts as an added protective layer. The third is a PVDF layered with two layers of the same tape. The fourth one is a PVDF which is folded into half. These PVDF films are affixed to a metal plate as shown in Figure 10 to Figure 12.

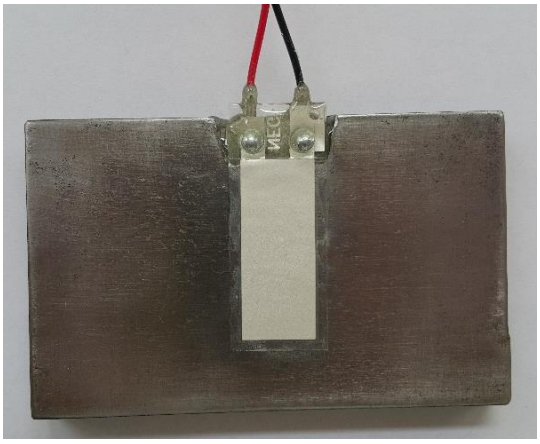

Figure 10. Prepared PVDF film with no additional protective layer

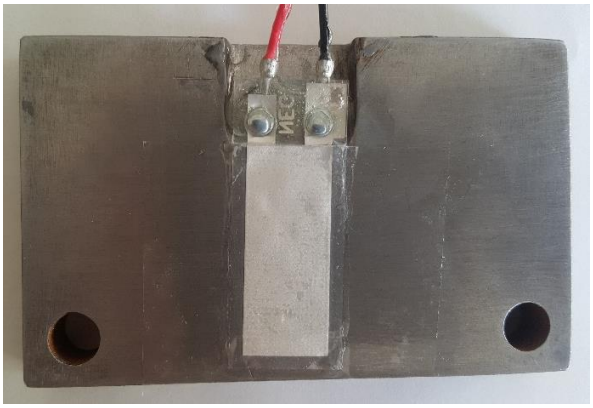

Figure 11. Prepared PVDF film topped with one layer of protective tape

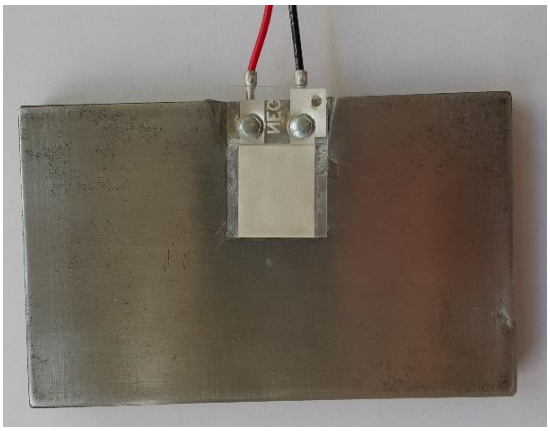

Figure 12. Prepared folded PVDF film fixed to a metal plate

Calibration

The direct data that can be obtained from the sensor is voltage. This voltage is proportional to the force or pressure acting on the sensor's surface [31]. However, since the area of impacting micro jets or bubble collapses are not uniform, using the pressure parameter will be difficult. Hence, the calibration will be carried out to convert voltage to force and not pressure.

Figure 13 displays the experimental setup during the calibration of the sensor. This was done by using the ball-drop test method adapted from the calibration work done by Hujer et. al. [44] on the same type of PVDF sensor. In this method, differently sized stainless steel balls are used. In this study, four balls weighing 0.253 g, 0.440 g, 1.043 g and 1.487 g are utilized. These balls are dropped from a known initial height h_1 to fall into the sensor. The ball with rebound to a height h_2. A camera with slow motion feature is used to capture accurately this rebound height since the ball bounces very fast that the height h_2 cannot be easily identified by the naked eye. The impact duration τ and maximum voltage U_{max} during the ball drop were measured using DAQ with LabView Signal Express software. These variables are indicated in Figure 14.

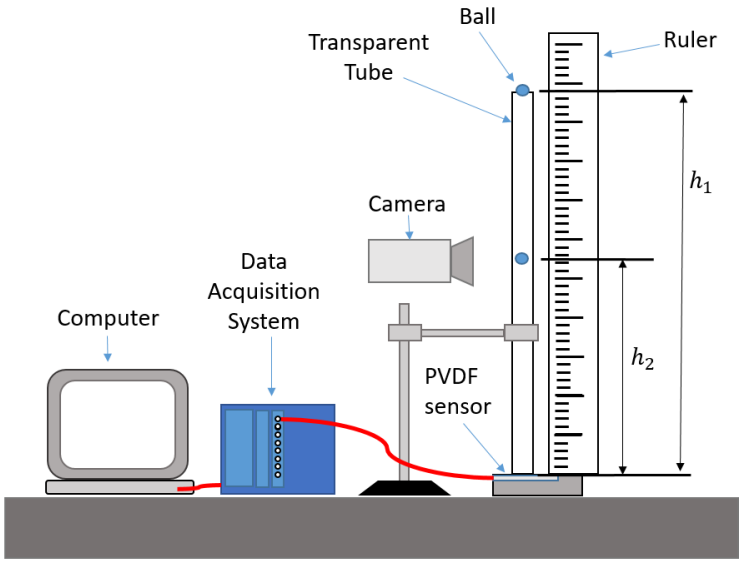

Figure 13. PVDF film calibration setup

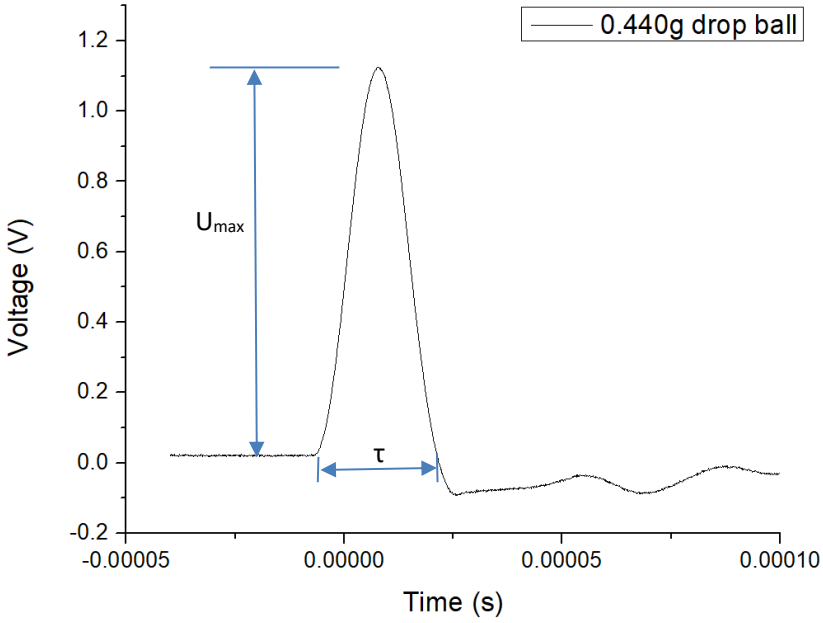

Figure 14. Sample signal when 0.440g of ball is dropped into the PVDF sensor from a height of 400 mm

Using the impulse-momentum theorem, the mean impact force can be obtained as

$$F_{mean} = \frac{1}{\tau}\int_{t1}^{t2} F(t)dt = \frac{m}{\tau}(v_1 + v_2) \quad (16)$$

where v_1 and v_2 are the velocities of the ball from point 1 and 2, respectively. It can be computed using the equation

$$v_{1,2} = \sqrt{2gh_{1,2}} \quad (17)$$

where g is the acceleration due to gravity and h is the height of the ball. The mean force calculated from the PVDF signal can be converted to maximum force using the following equation

$$F_{max} = 2 \cdot F_{mean} \quad (18)$$

The calibration curve can be obtained from plotting a graph of the maximum voltage (U_{max}) obtained from the PVDF signal versus the maximum force calculated. The slope of the fitting curve in this graph is the calibration constant or the sensor sensitivity which will be used for converting voltage reading to its corresponding force value.

3.1.2.2 Hydrophone

A PVDF hydrophone needle (RP-Acoustic) is used to determine the pressure in a far field. It has a sensitivity of 29mV/ MPa with amplifier set at 40 dB. This sensor is also connected to DAQ device for data gathering.

3.2 Experimental Setup

The ultrasonic device, PVDF film, and the data acquisition instrument are setup as shown in the Figure 15. The PVDF film secured at the top of a metal plate is placed at a stand-off distance of 5 ± 0.2 mm below the horn. This distance was fixed in the setup by using a standard measuring gage block (Somet). The sensor is submerged in water contained in a transparent container. Water is filled up such that the horn is dipped at 45 ± 2 mm depth from the water surface. The temperature is maintained at 25 ± 2 °C all throughout the experimental runs.

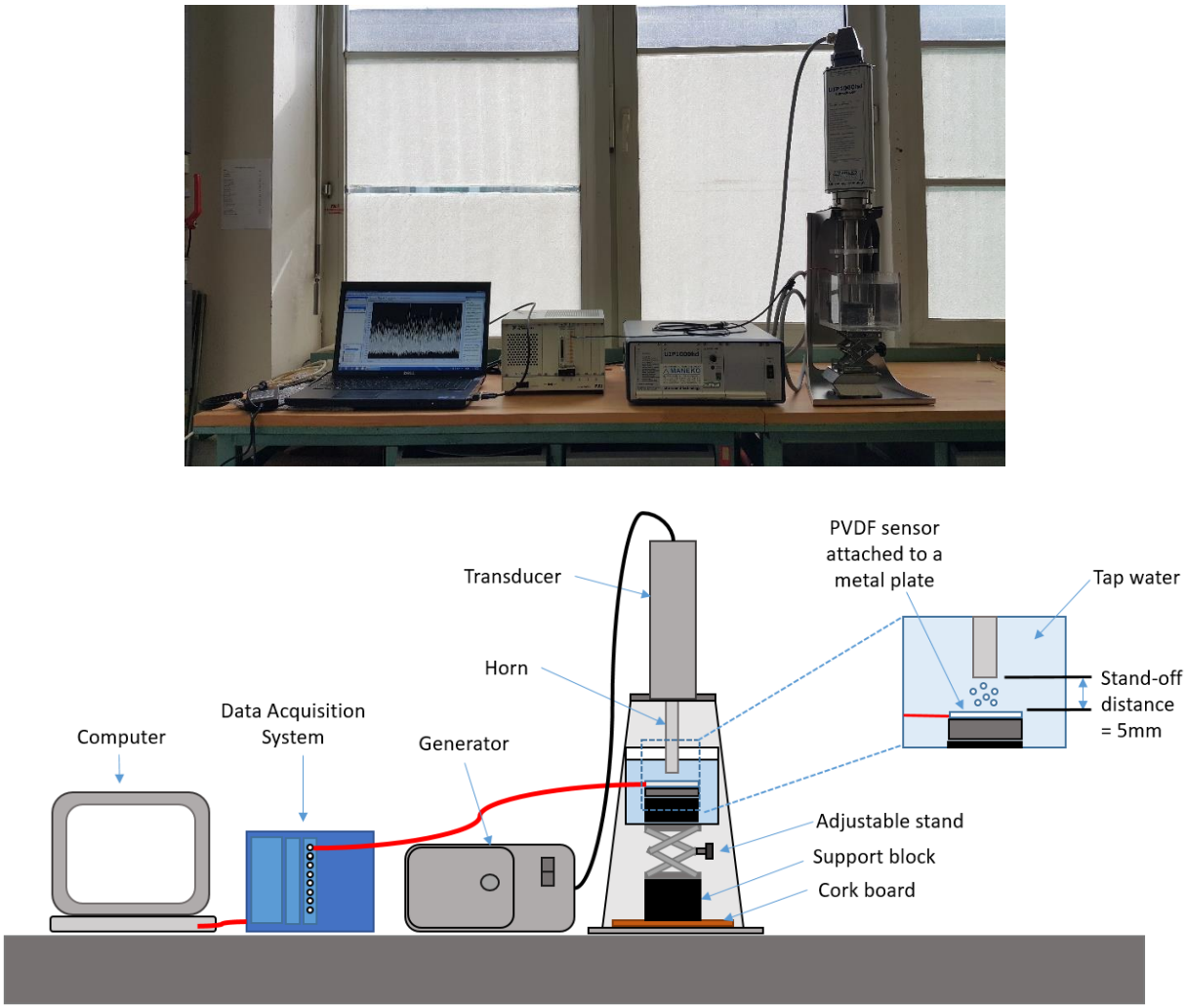

Figure 15. Ultrasonic cavitation experimental setup

To get the impulsive signal from the cavitation, the ultrasonic transducer is turned on and data were taken at a duration of 15 ms. The PVDF film and the hydrophone signals are both obtained at 60 MS/s rate using the DAQ.

In order to establish a statistically sound data, the optimal number of trial runs was determined. This was done by doing 10 experimental runs having 15 ms length each run. Each run is cumulatively added to each other until reaching 150 ms length of sampling time. Trend on the peak rate vs. peak amplitude was examined as duration length is extended. The number of runs needed

to achieve a stable unfluctuating data served as the basis for the number of trial runs for the proceeding aggressiveness test.

Moreover, identifying the optimized configuration of the PVDF film is also a subject of this study. Sensitivity of the aforementioned different configurations were assessed to be able to determine the most appropriate setup for the next tests.

Aggressiveness of cavitation was then evaluated by determining the force signals from the cavitation when the ultrasonic horn vibrates at different amplitude. The chosen optimized PVDF configuration was subjected to 50, 75 and 100% of the 57 μm amplitude of the ultrasonic transducer.

3.3 Post-Processing of Signals

The data that can be obtained from the PVDF is in the form of amplitude (voltage) vs time (s) graph as shown in Figure 16. The data here was obtained using bare PVDF film affixed to the metal plate as illustrated in Figure 10.

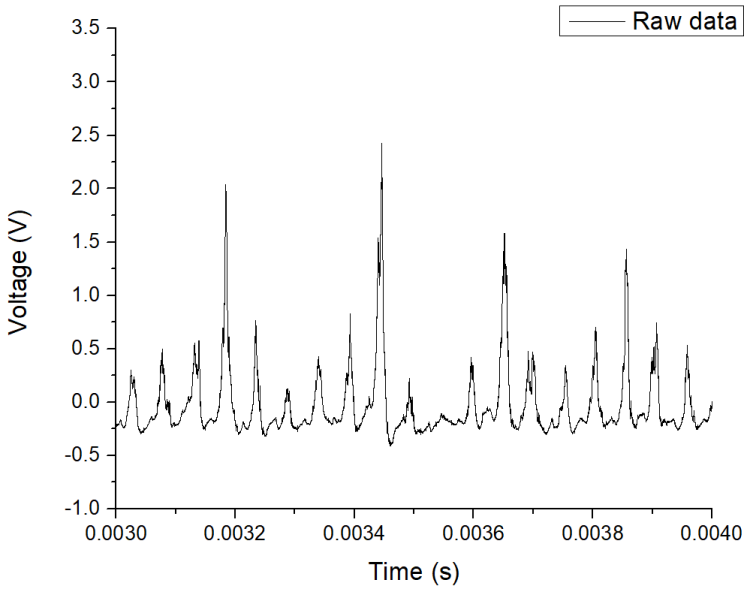

Figure 16. Raw signal as obtained from DAQ

To eliminate noise in the peaks, Savitzy-Golay filter is used to smoothen the signal. Figure 17 and Figure 18 show the effect of this filter.

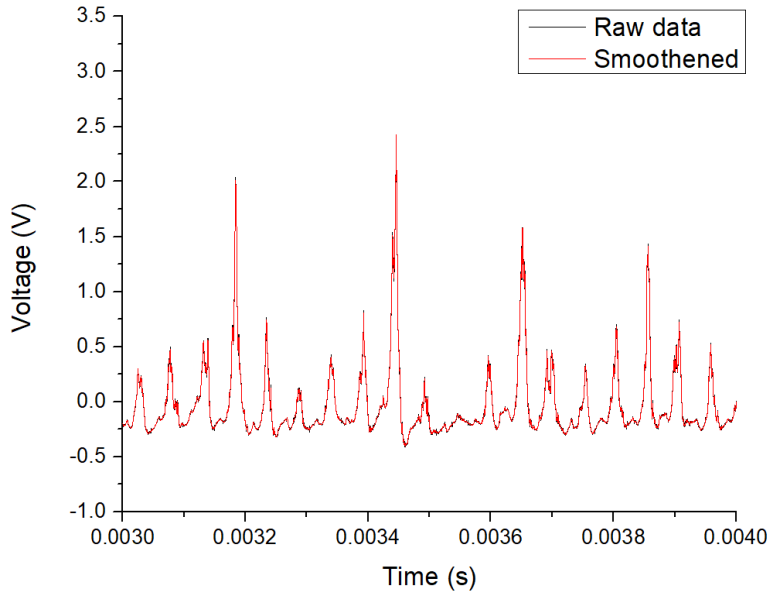

Figure 17. Smooth filtering of the raw signal

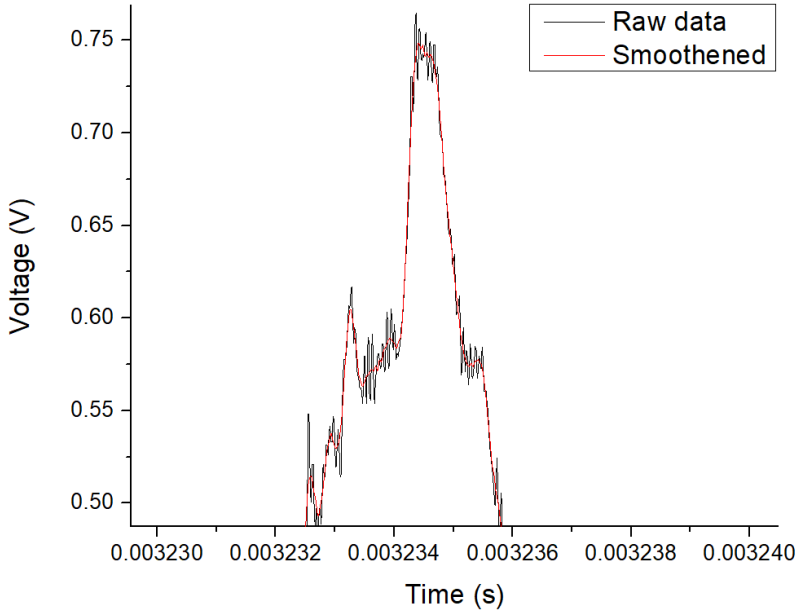

Figure 18. Zoom-in view of the effect of filter

The zero baseline is set such that it is at the top of background noise. To do this, the frequency count per 0.01V voltage range is calculated. The voltage value with the highest number of count correspond to the level where most of the noise falls.

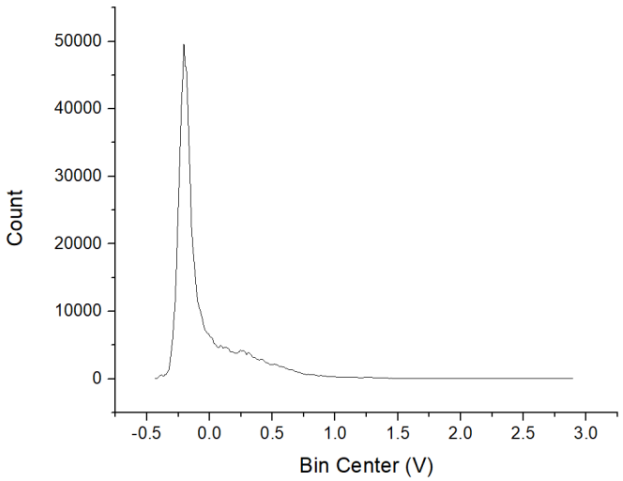

Figure 19. Data frequency count per 0.01 V bin range

In order to set the baseline just above this noise, the derivative of this count vs bin center (V) graph is calculated. The identified minimum derivative value from this graph is set as the baseline of the signal and this will serve as the zero when identifying the signal peak voltage value. For the case in Figure 20, the minimum derivative value is -0.155 V.

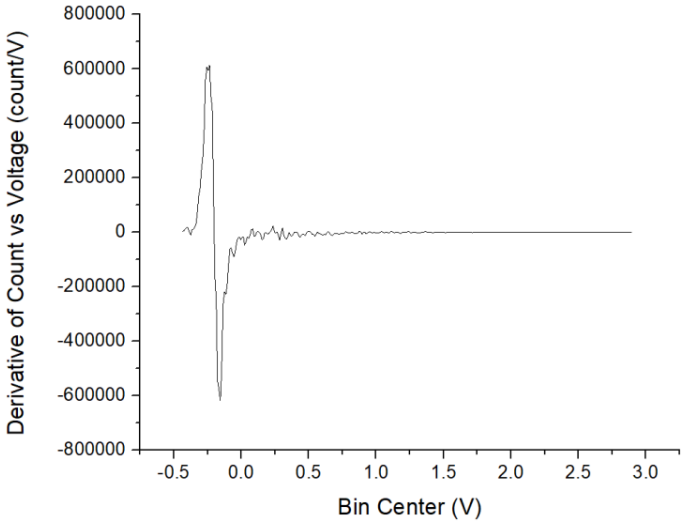

Figure 20. Derivative of data frequency count per 0.01 V bin

The determined baseline is presented in Figure 21 whose value is subtracted from the original signal to set this line as the zero. The resulting graph is shown in Figure 22. From this, the peak height is identified.

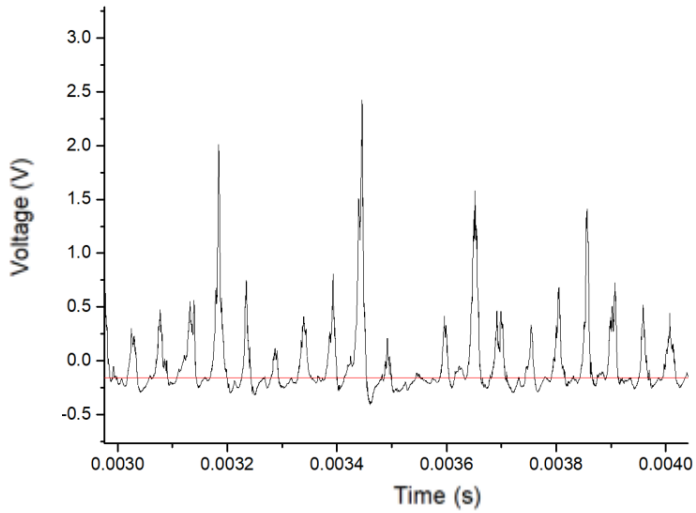

Figure 21. Red line is the baseline

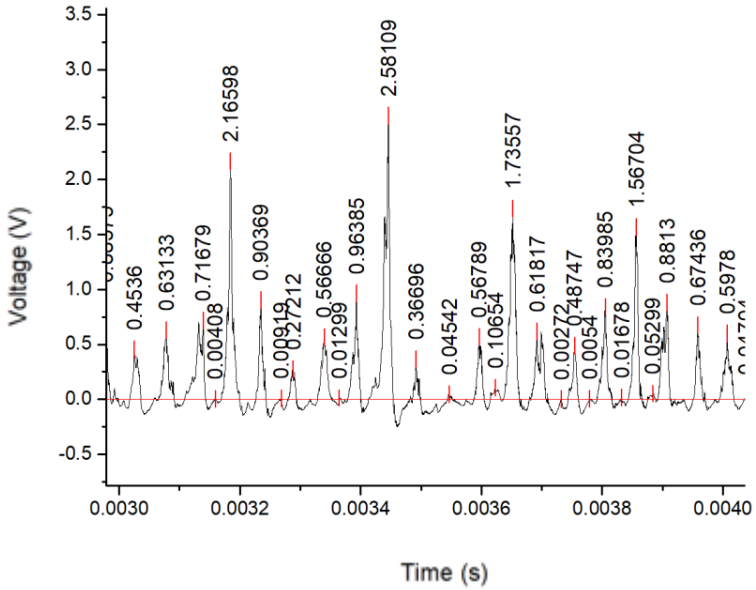

Figure 22. PVDF signal after offsetting the baseline to 0 V.

This method of processing of electrical signal is applied to all experimental data in identifying the resulting peak voltages induced by each bubble collapse.

4 RESULTS AND DISCUSSION

The electrical signals produced by the PVDF sensor from the bubble collapses are recorded and impact peaks are identified for the various experimental setup having different parameters. Based from this, analysis is carried out to better explain bubble collapse impact from a cloud cavitation produced by ultrasonic waves.

4.1 Signals for Different Sample Duration Length

A PVDF sensor with one layer of tape is exposed to ultrasonic cavitation for exposure time of 15 ms for 10 sample runs. Figure 23 shows the cumulative peak rate per voltage after assessing the peaks of the voltage vs. time signal. The peak rate axis data is in cumulative form such that each rate value is the peak rate for values greater than the corresponding voltage. The area accounted for the calculation of peak rate is area of the sensor.

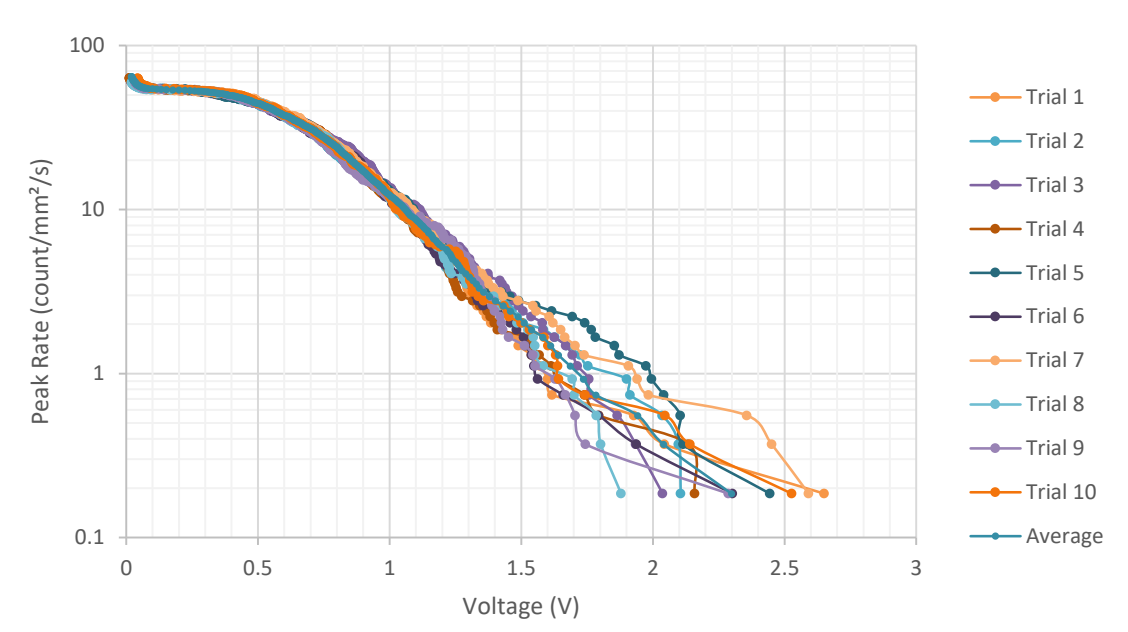

Figure 23. Signals from PVDF with one layer of tape after being exposed to 50% vibration amplitude condition

The use of very high sampling frequency rate of 60MS/s which results to a taking huge number of data and the avoidance of PVDF sensor damage are the factors that limit this study from taking a long duration time signal sample at one experimental run. In order to get a more accurate overall picture of what the data signal would look like for a longer run, each 15ms sample run is added into each other to reach a longer sample run, i.e, the 15ms data is from the Trial 1, 30ms data is from the addition of Trial 1 and Trial 2, and so on until reaching 150 ms which is the sum of all sample runs from Trial 1 to 10. Figure 24 shows the resulting data.

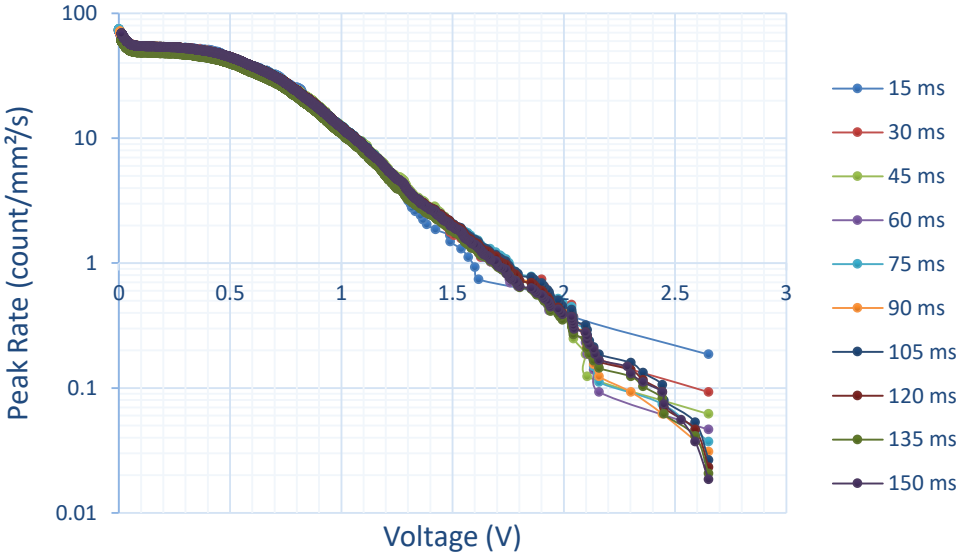

Figure 24. Cumulative peak rate for different sample duration length

Based on this, it can be observed that after summing 3 runs, the trend goes to form a linear relationship of peak rate and voltage. This attained linear part in the linear-logarithmic scale graph is also evident on findings from other researches [30] [31] [34] [45]. This goes to show that in order to attain this linear trend of peak rate vs. voltage in linear logarithmic scale, a number of samples must be taken to have a good representative data of the cavitation phenomena. In this sampling length of 15 ms set, a minimum of 3 samples must be obtained and this will serve as a basis for the number of sampling run for the proceeding parts of the experiment.

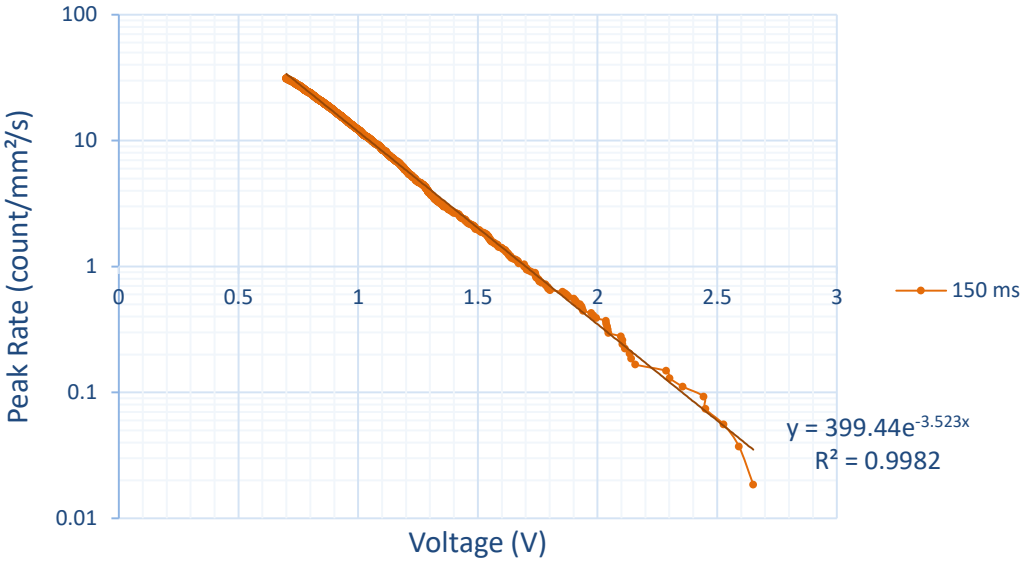

Figure 25. Linear part of the cumulative peak rate plot for 150 ms sample duration length

The linearity in the linear-logarithmic scaled graph denotes an exponential law relationship of the type

$$\dot{n} = \dot{n_0} e^{-\frac{U}{U_o}} \tag{19}$$

where $\dot{n}$ is the peak rate, $\dot{n_0}$ is the reference peak rate, U is the peak voltage, and U_o is the reference voltage. For this case, the values of $\dot{n_0}$ and U_o are 399.44 peak/mm^2/s and 0.284 V, respectively.

4.2 Different PVDF Configuration

The PVDF films were prepared in four different ways, namely, film with no additional protective layer tape, film with one layer of tape, film with two layers of tape, and film folded into half. All these films were exposed to 50% vibration amplitude. The resulting post processed signals as described in Section 3.3 are as follows:

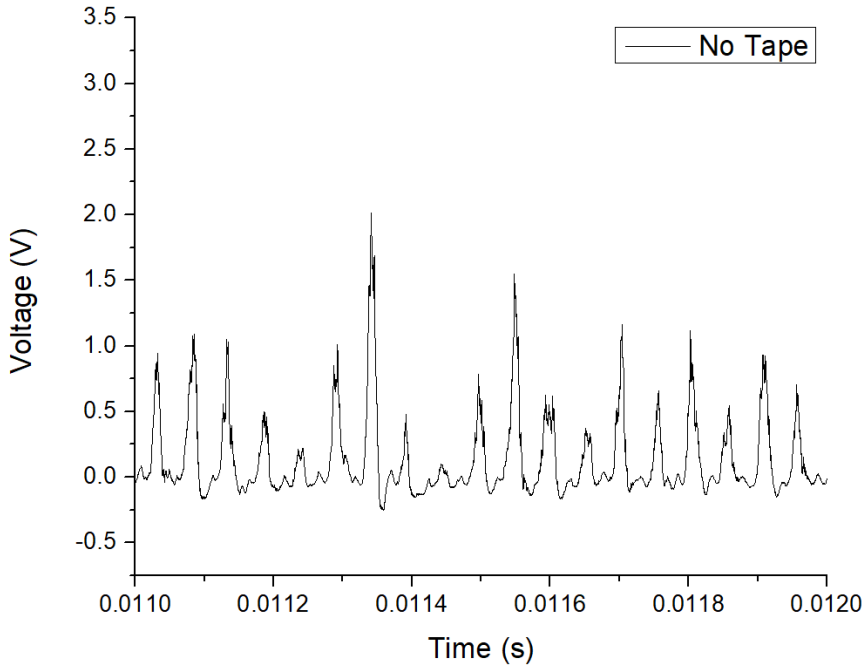

Figure 26. PVDF signal for PVDF film with no additional layer of tape

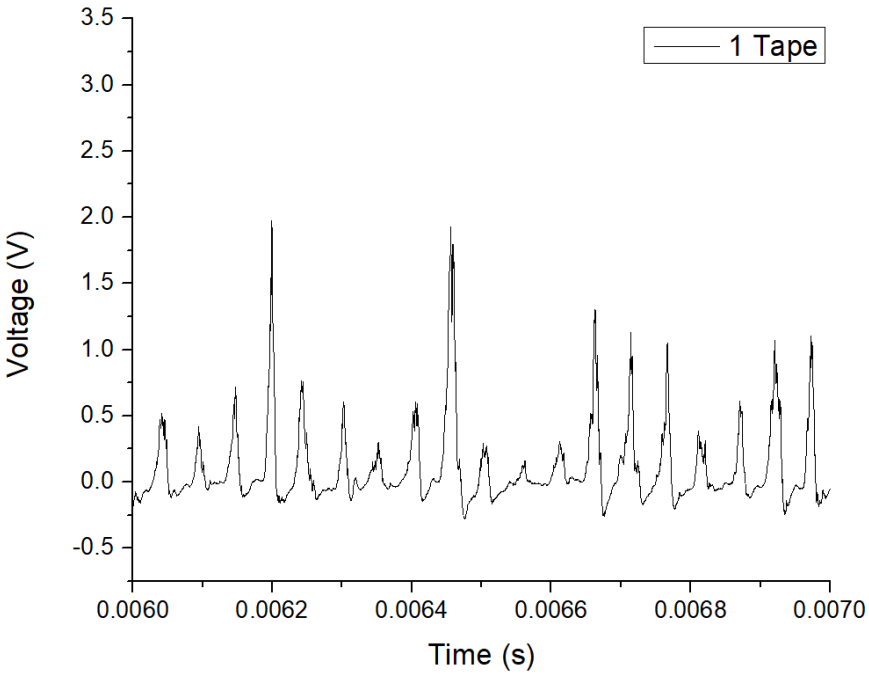

Figure 27. PVDF signal for PVDF film with one layer of protective tape

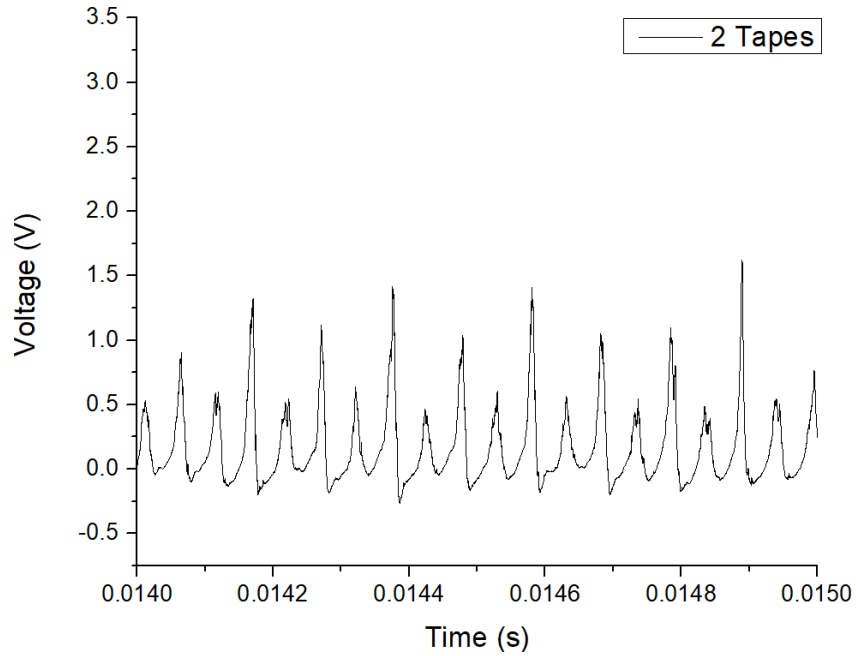

Figure 28. PVDF signal for PVDF film with two layers of protective tape

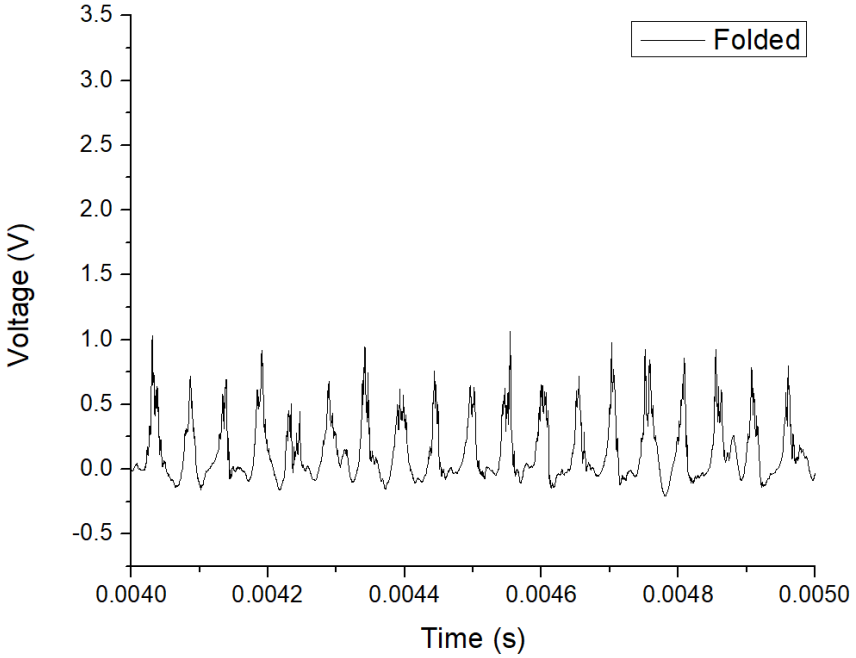

Figure 29. PVDF signal for the folded PVDF film

These signals have almost same overall feature except for the varying voltage amplitude. These signals also show similarity to the pressure signal data gathered by Singh et. al. [30] who used pressure transducer for measurements. This proves that the signals obtained from PVDF sensor are correct.

Figure 30 to Figure 32 illustrate the cumulative peak rate vs voltage graph for the different PVDF film configurations which were subjected to ultrasonic cavitation for five trial runs. The results for the PVDF film with one tape is shown in Figure 23. The plot for every trial runs almost coincides with each other but it appears to slowly deviate as it approaches the maximum voltage read per trial run. The maximum standard deviation recorded is 0.31 V for the PVDF with no additional tape, 0.25 V for PVDF film with one layer of tape, 0.11 V for PVDF film with two layers of tape and 0.29 V for the folded PVDF film. This denotes that there is a high variation on the recorded maximum bubble collapse impact per trial run.

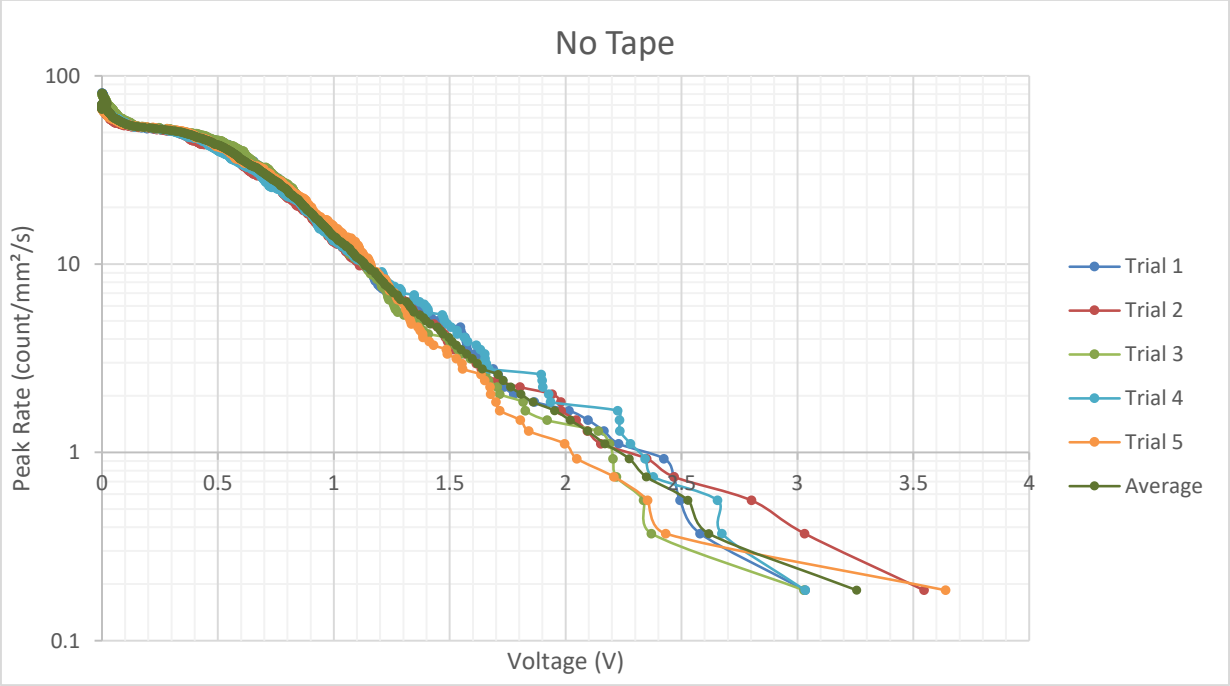

Figure 30. Cumulative peak rate per voltage for PVDF with no additional protective tape

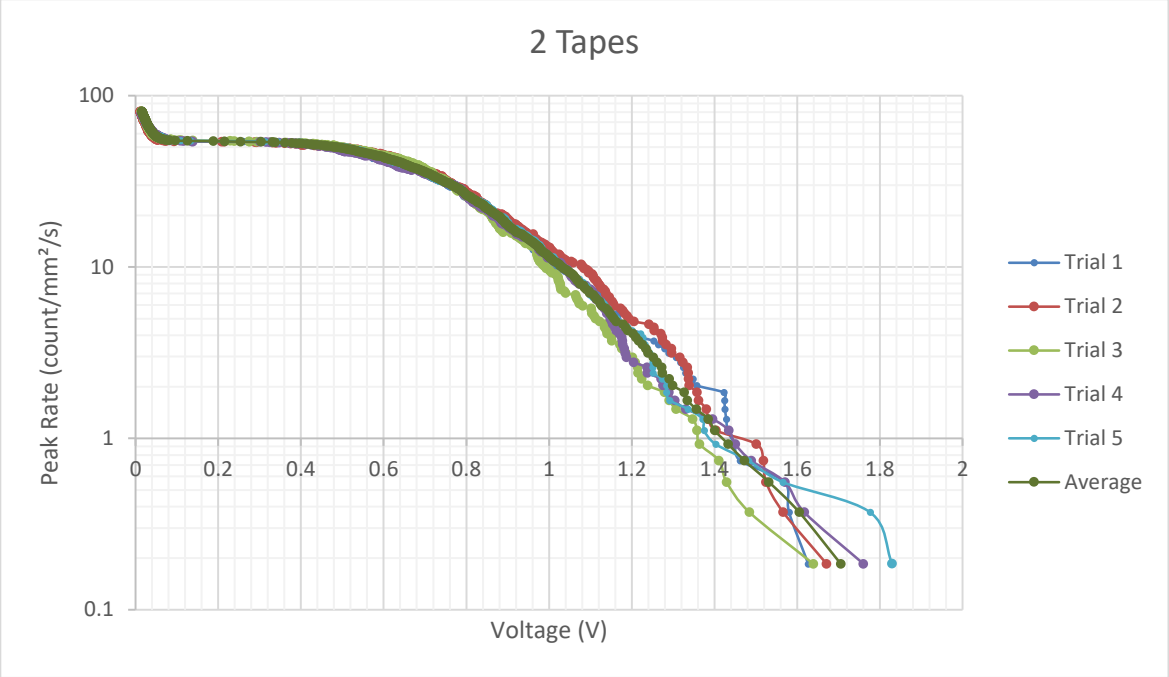

Figure 31. Cumulative peak rate per voltage for PVDF with two layers of tape

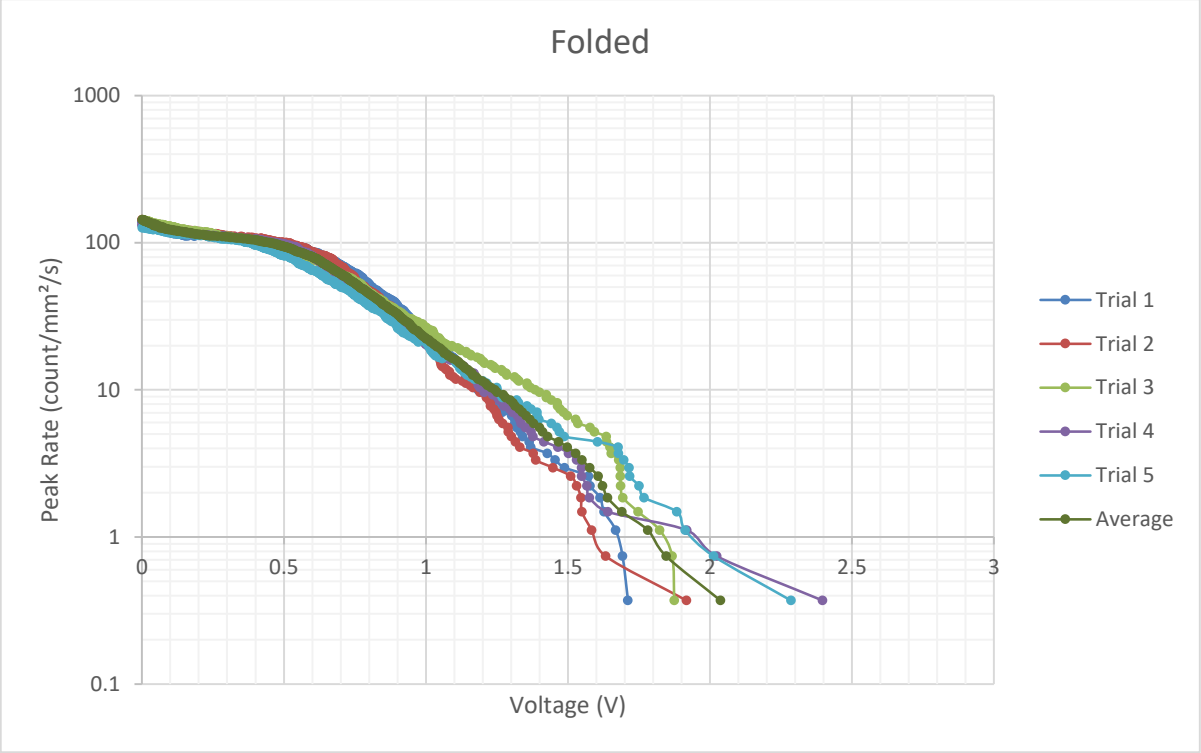

Figure 32. Cumulative peak rate per voltage for folded PVDF

The compiled data signals for the four PVDF configurations are plotted in Figure 33 in terms of their average values for the five experimental runs.

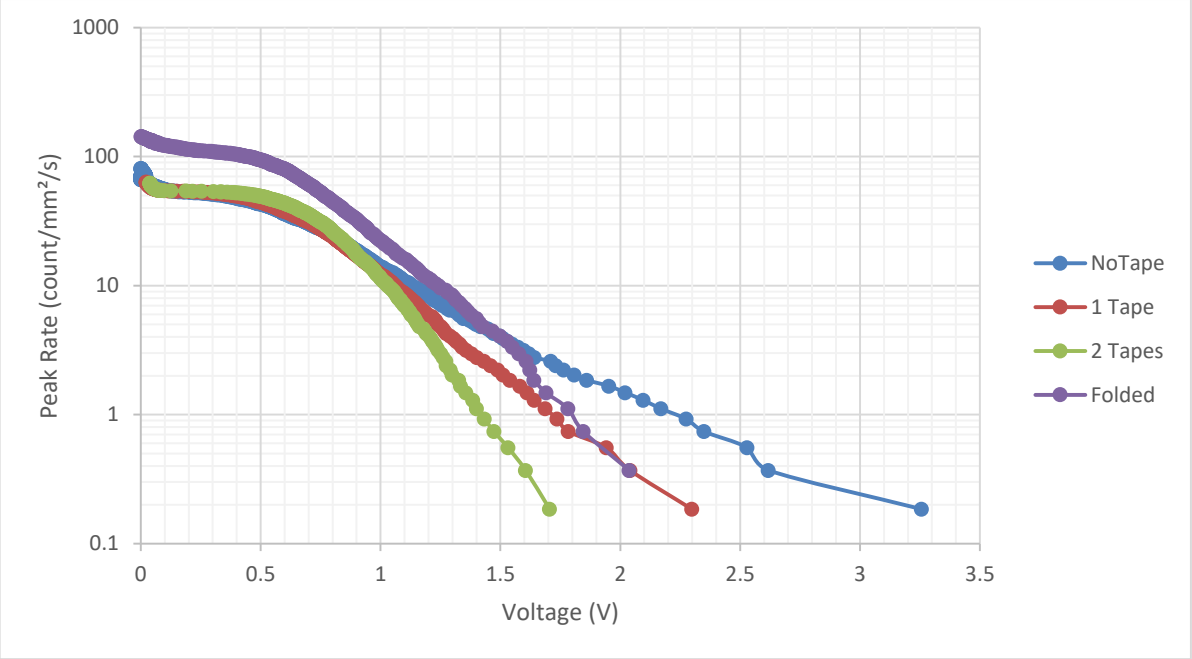

Figure 33. Cumulative peak rate histogram for different PVDF configurations

Figure 33 shows that the PVDF with no tape is able to generate highest electrical voltage among other configurations. This means that this PVDF setup offers the highest sensitivity to cavitation impacts. This is followed by PVDF with one layer of tape and then two layers of tape. This denotes that the added protective layer can significantly decrease the sensitivity of the sensor in detecting bubble collapse impacts. On the other hand, the folded PVDF recorded higher total peak count. The area used for this is only half the area of the other PVDF configurations. According to an experimental study conducted by Paepenmöller, et. al. [39], the bubble impacts decreases as the distance from the center of the horn increases. Hence, for the case of the PVDF with no tape, 1 tape and 2 tapes setups where the whole film is laid flat on the metallic base plate, areas on the extreme end of this rectangular PVDF sensor does not get much bubble impacts as the one in the center which is directly located below the area of the horn. Due to this, bubble impact density recorded in the folded PVDF is the highest among the three configurations but only for low voltage values.

As the voltage peak value is increasing, the curve in the plot for this folded PVDF is observed to go slightly lower than the PVDF film with one layer of tape. This then means a decrease of sensitivity performance of the sensor. During the preparation of the PVDF, the folding process might have caused internal damage to the film thus resulting to less sensitivity effect. If there is breakage of film along this fold, then only half part of the PVDF is effectively working. The half which is located above is serving as wall between impact and the working PVDF layer. This "dead" PVDF layer is decreasing the sensitivity of the sensor with the same way as what a protective layer does. Additionally, if the PVDF film is essentially cut into half because of this damage along the fold, the capacity of the piezoelectric sensor is decreased thereby dramatically reducing the intensity of the electrical signal and its sensitivity.

The most suitable PVDF film configuration should have a high sensitivity and at the same time be able to withstand cavitation impacts. The PVDF film with no tape layer is clearly the most sensitive sensor but this is highly prone to damage. The PVDF film with one layer of tape exhibits to have the second highest sensitivity and was also proven durable when it was exposed to 10 trial runs. Therefore, if balance of good sensitivity and durability are to be considered, then the PVDF film with one layer of tape is deemed to be the best suitable configuration for the next experimental runs.

4.3 Determining Impacts at Different Amplitude Level

The PVDF film with one layer of tape is used to assess the aggressiveness of cavitation at different intensity. It was subjected to 50%, 75% and 100% of 57 μm vibration amplitude of the ultrasonic horn. This film was calibrated before and after conducting the experiment and the calculated calibration constant is 6 mV/N (see Section 4.6 for further details of the results of calibration).

Figure 34 and Figure 35 show the data at 5 trial runs done at a 75% and 100% vibration amplitude, respectively. The data in Figure 23 for 50% vibration amplitude will still be used here for comparison. Figure 36 shows the compiled data to evaluate the effect of different vibration amplitudes on the peak rate.

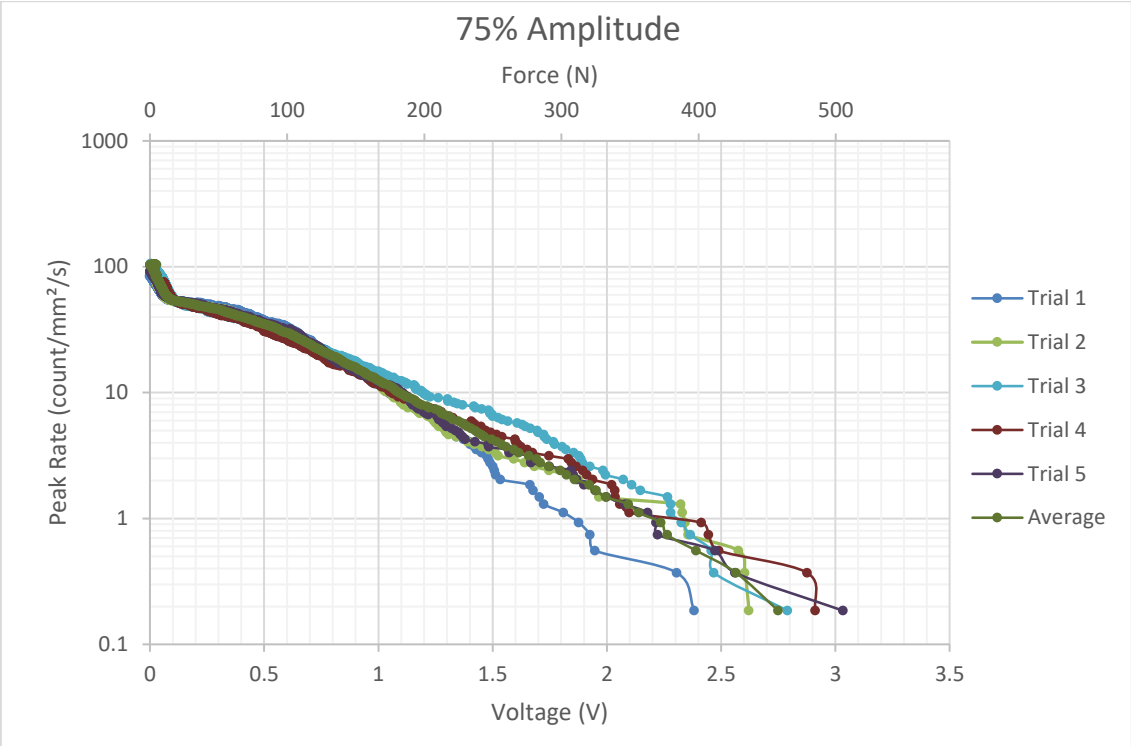

Figure 34. Cumulative peak rate vs. peak voltage obtained at 75% vibration amplitude

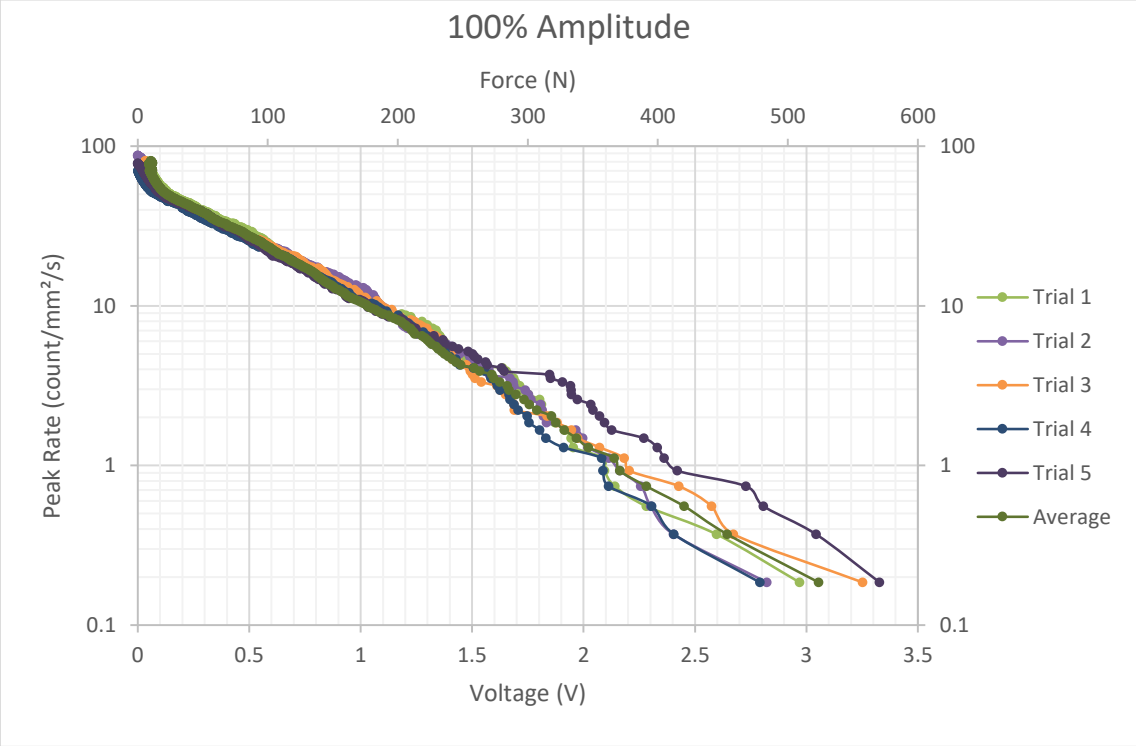

Figure 35. Cumulative peak rate vs. peak voltage obtained at 100% vibration amplitude

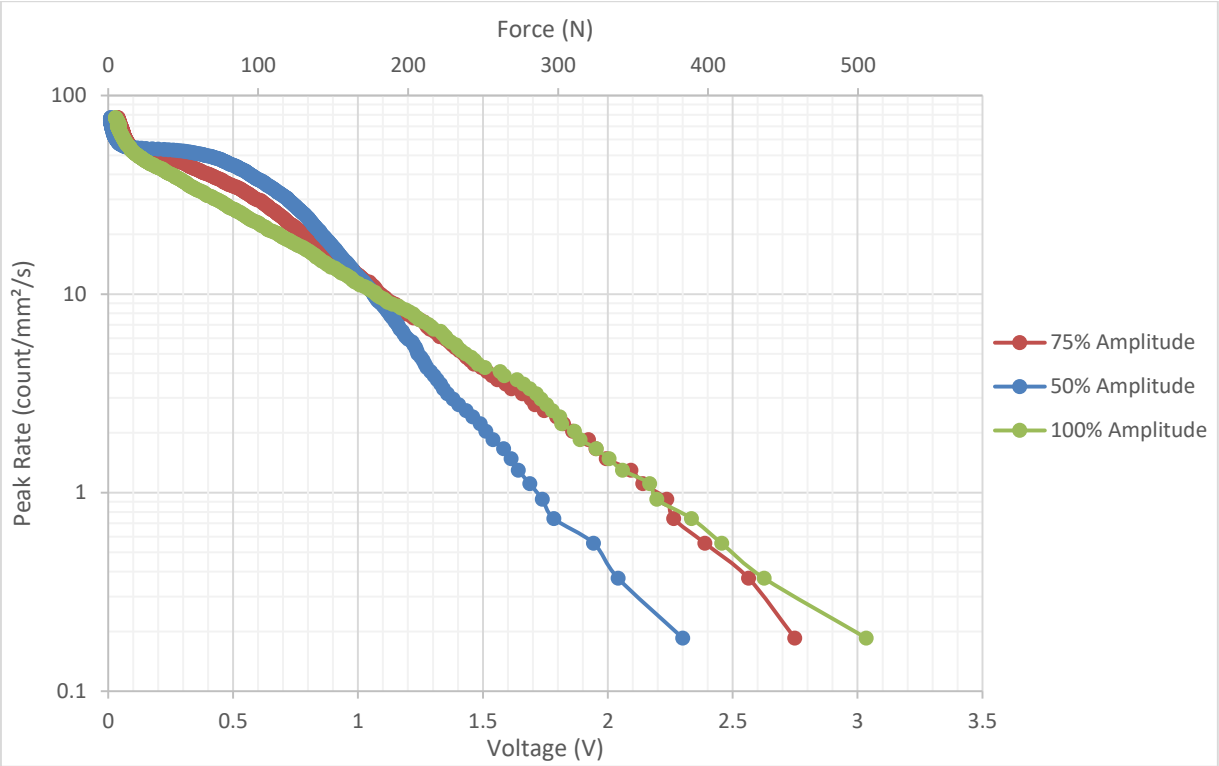

Figure 36. Cumulative peak rate for different vibration amplitude

As displayed in Figure 36, the increase of the vibration amplitude leads to greater rate of detected high voltage peaks. This implies that the aggressiveness of cavitation is enhanced when vibration amplitude is set to a high level. This then suggests that the high compression force applied to the water aids in the generation of bubbles that collapse more intensely. This result coincides with the findings of other research [35]. However, at low voltage readings, the lower vibration amplitude is seen to produce higher peak rate.

It can also be noted that the curve in the linear-logarithmic scale graph in all cumulative peak rate for different amplitude level consists of a linear and a non-linear region. The non-linear part is seen in the region of very low voltage values. This voltage values close to zero can be regarded as noise and/or impacts from collapse of very small sized bubbles. This can be considered to create negligible effects unable to form pits on the material.

Same as discussed in Section 4.1, the linearity in the logarithmic scaled graph supports an exponential law following equation 19. If the voltage variable is converted to force load, the exponential law will be further deduced as

$$\dot{n} = \dot{n}_0 e^{-\frac{F}{F_o}} \tag{20}$$

where F is the peak impact force and F_0 is the reference force. Table 1 details the derived values of the constants $\dot{n}_0$ and F_0 for various vibration amplitude.

Table 1. Constants for the exponent law relationship of force and peak rate

Vibration level with respect to 57µm amplitude	Reference peak rate, $\dot{n}_0$ [peaks/mm^2/s]	Reference force, F_0 [N]
50%	362.34	50
75%	112.79	76.9
100%	82.6	83.3

The PVDF signals taken from different vibration amplitude level are presented in Figure 37 to Figure 39. These were also post-processed as described in Section 3.3. The asterisk (*) symbols were placed to mark the dominant peaks that are noticed to be occurring after some ultrasonic horn vibration cycles. These high peaks are seemingly less pronounced in low vibration amplitude and becomes more noticeable at higher vibration amplitude setting.

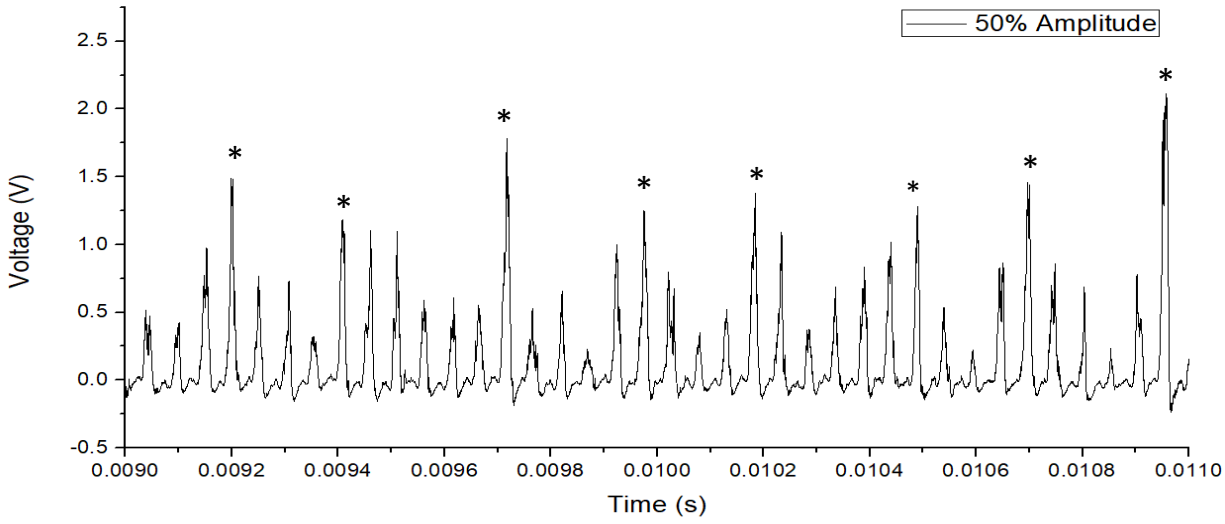

Figure 37. Signal from PVDF sensor with one layer of protective tape exposed to 50% vibration amplitude.

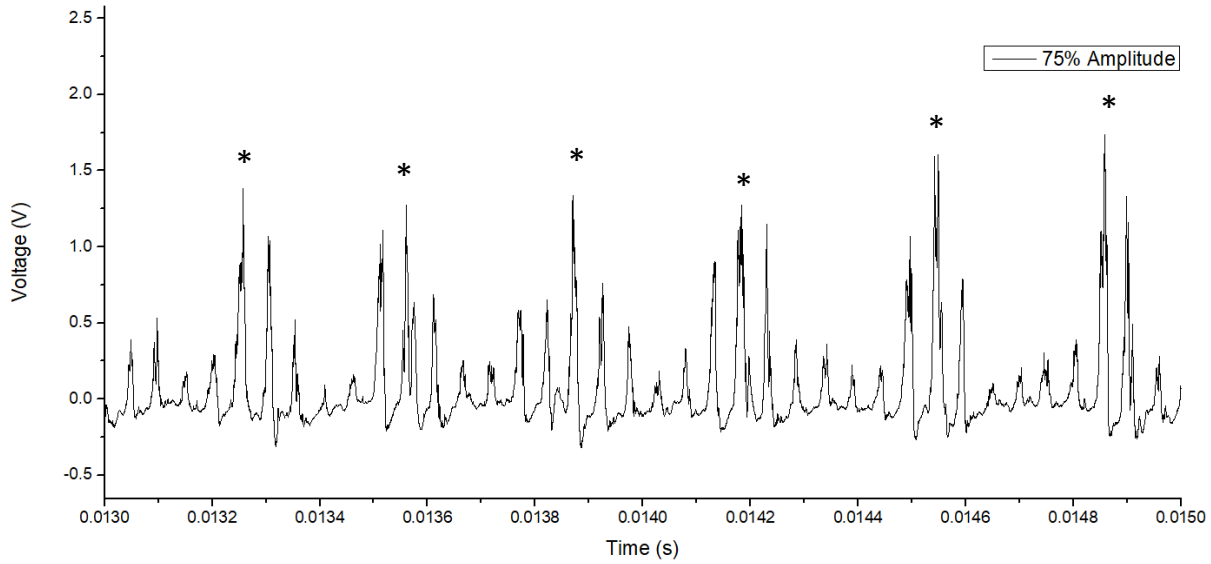

Figure 38. Signal from PVDF sensor with one layer of protective tape exposed to 75% vibration amplitude.

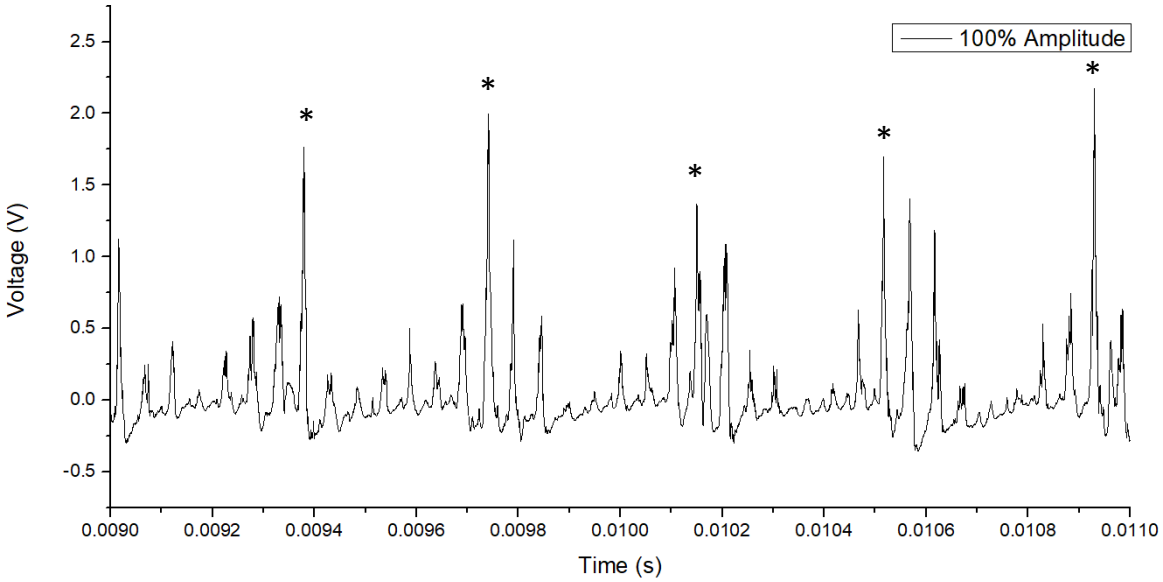

Figure 39. Signal from PVDF sensor with one layer of protective tape exposed to 75% vibration amplitude.

Similar observation can also be seen on the recorded signals from the bare PVDF film with no additional protective layer of tape as seen on Figure 16. To further expound on this, Fast Fourier Transform (FFT) is performed to determine the frequency of this dominant peak occurrence. The FFT frequency domain graphs are seen in Figures Figure 40 to Figure 42 for the different vibration amplitude.

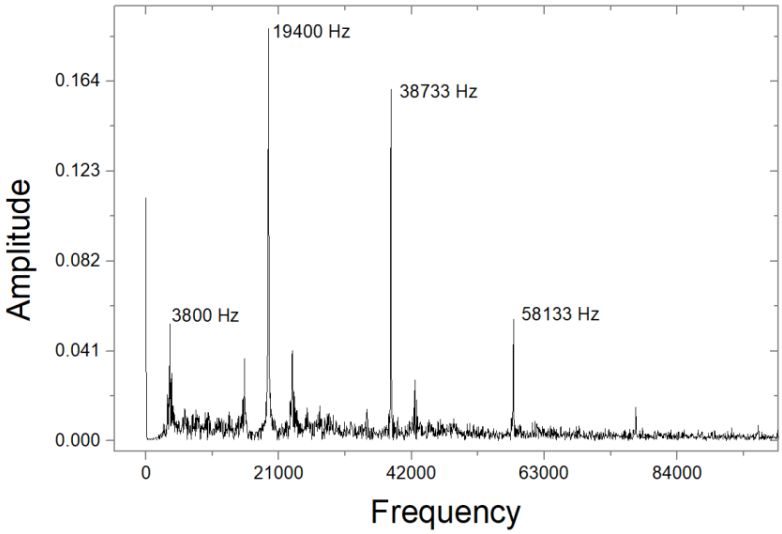

Figure 40. FFT for 50% vibration amplitude

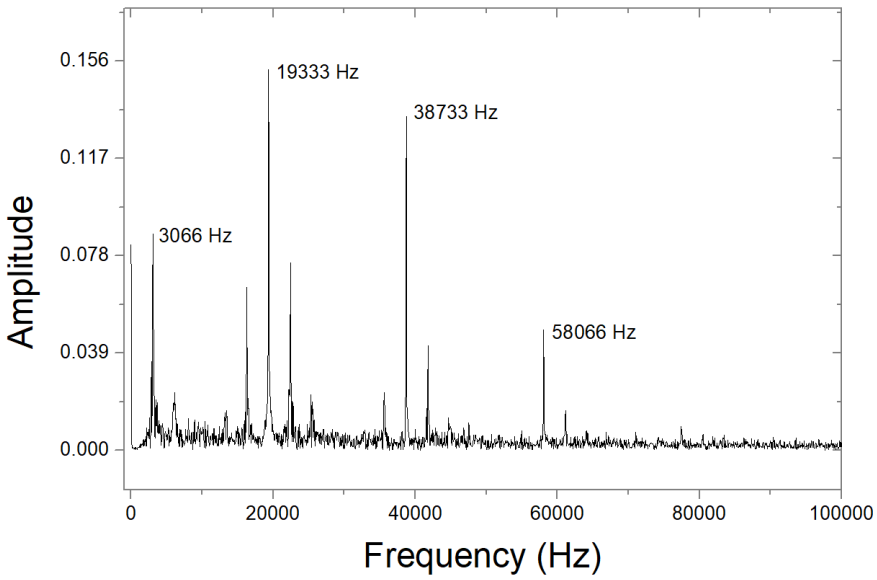

Figure 41. FFT for 75% vibration amplitude

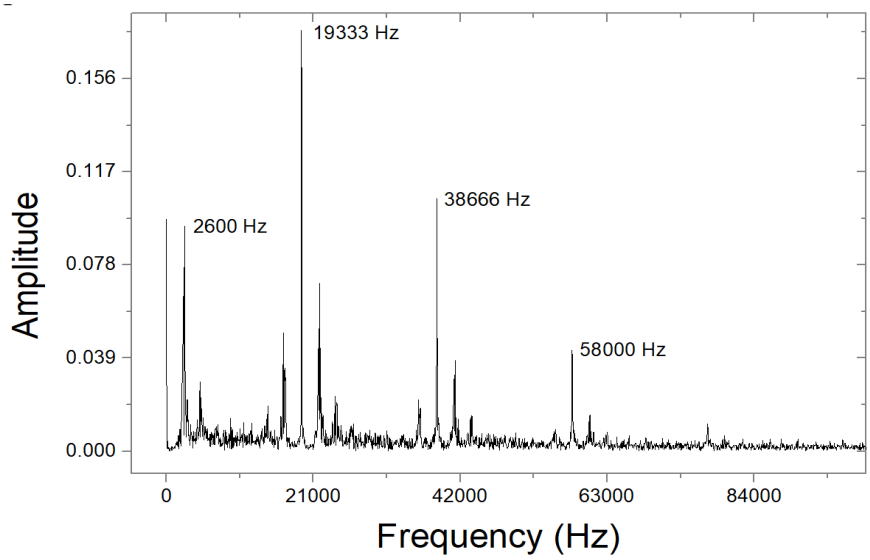

Figure 42. FFT for 100% vibration amplitude

The PVDF exposed to 50% amplitude shows signal with a high amplitude at 3,800 Hz which corresponds to approximately 5 times of the cycle of the ultrasonic horn vibration. The next dominant FFT peak occurs at 19,400 Hz which is almost equivalent to the set horn vibration frequency which is 20,000 Hz. Sidebands are visibly occurring at the interval of 3,800 Hz indicating modulation of these signals. Other prevailing peaks in FFT graphs occur at 38,733 Hz and 58,133 Hz which are just the harmonics of the horn frequency. Almost similar trend is seen on the FFT data from signal of PVDF film exposed to 75% and 100% vibration amplitude. However, the frequencies at which dominant high voltage peaks are observed are at 3,066 Hz and 2,600 Hz for the 75% and 100% vibration amplitude, respectively which suggests that high peaks occur averagely at every 6.5 and 7.5 times of the horn vibration period.

Table 2. Frequency of prominent high peak occurrences for different vibration amplitudes

Vibration Amplitude	Trial	High impact frequency (Hz)	Average frequency (Hz)	Standard Deviation
50%	1	3733	3719.6	56
	2	3733		
	3	3666		
	4	3666		
	5	3800		
75%	1	3066	3119.4	128
	2	3266		
	3	2933		
	4	3199		
	5	3133		
100%	1	2600	2506.4	89
	2	2600		
	3	2466		
	4	2400		
	5	2466		

Table 2 summarizes the frequency of the notably high impacts for different vibration amplitude level tested for 5 number of trials. It shows that these strong impacts occur at a frequency which decreases when the vibration amplitude is increased. These high impacts denote presence of large bubble cavity and this is supported by findings of Žnidarčič et. al. [43] who, through the use of high-speed camera and hydrophone, have observed that the cyclic period of growth and collapse of a large attached cavity on the ultrasonic horn increases with higher power, which is also same as increasing the amplitude. This may indicate that the dynamics of the large cavity follows the Rayleigh collapse time rather than the ultrasonic horn driving period. The frequency at which the large cavity collapse arises can then be estimated to be equal to the inverse of twice the Rayleigh collapse time ($f = 1 / (2\tau)$).

The occurrence of significant high impact peaks at a certain frequency other than the frequency of the horn vibration also coincides well with the experimental findings of Birkin et. al. [46] who utilized laser scattering and high speed imaging to identify that a large bubble cluster is growing at the tip of the horn and this collapses every three to four cycles of the frequency of the horn.

After its collapse, presence of short-lived cloud of small bubbles is observed. These events match well with the recordings of the PVDF film wherein it is evident most specially at 100% vibration amplitude condition that a series of small voltage peaks are observed every after a significantly high peak voltage is read. The occurrence of a periodic large voltage reading from PVDF sensor verifies the presence of a large cluster of bubbles which collapses after some cycles of the horn vibration.

All these findings also prove a good agreement of results when different measuring instruments are used, namely, the PVDF sensor utilized here and the fast imaging instruments as employed by Žnidarčič and Birkin.

In all vibration amplitude conditions, the highest peaks in FFT arise at roughly 19,333 Hz which is close to the set 20,000 Hz oscillation frequency of the horn. Therefore, the collapse of bubbles, may it be weak or strong impact, mostly occurs at each vibration excitation of the ultrasonic horn.

4.4 PVDF Signal with No Load

Signal from the PVDF was obtained when it is submerged in still water with no vibration excitation of the horn. Signal was also taken when the film is exposed to only still air. These raw signals are seen in Figure 44 and Figure 45.

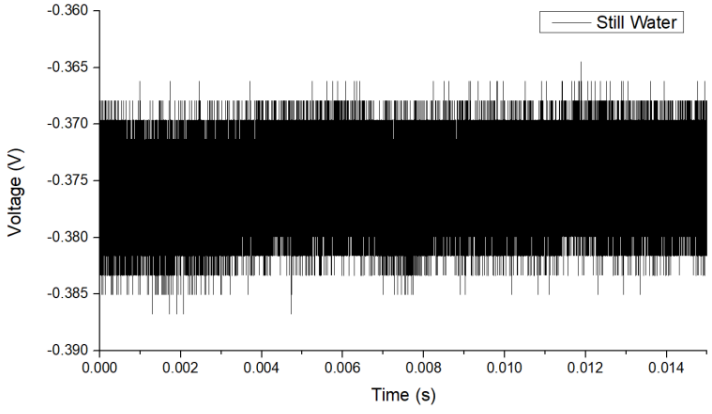

Figure 43. Raw signal from PVDF exposed to still water condition. This data taken is for 15ms sampling length

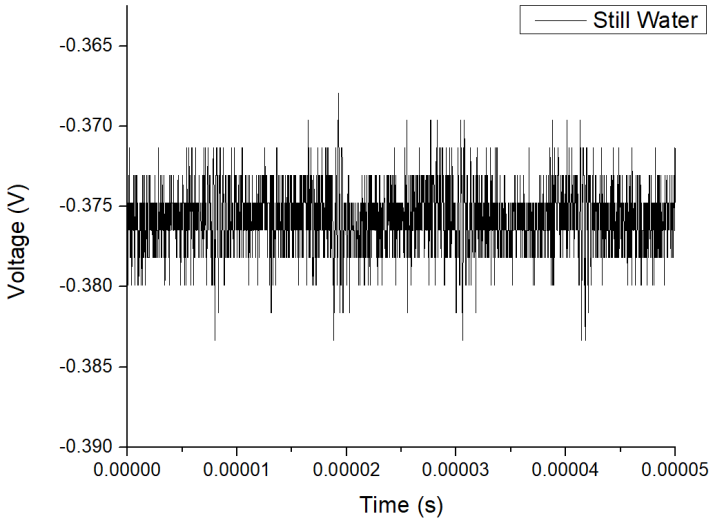

Figure 44. Raw signal from PVDF exposed to still water condition. Data is taken for 0.05 ms sample duration length

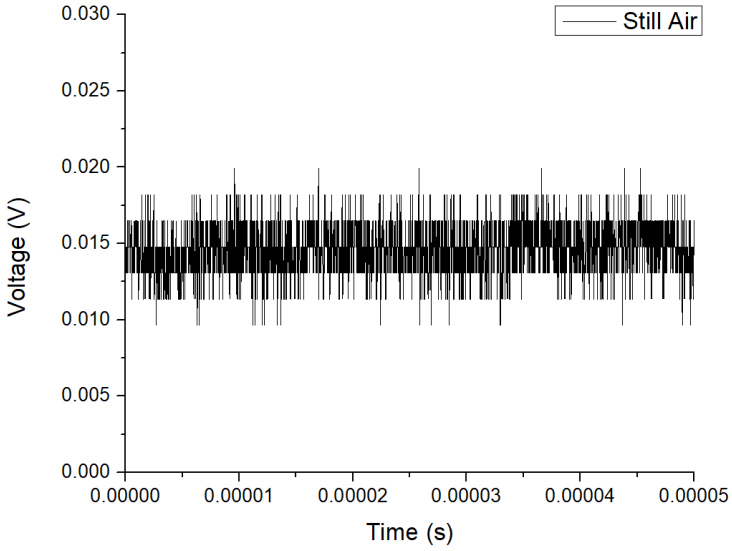

Figure 45. Raw signal from PVDF exposed to still water condition

Both these raw signals seemingly fluctuate with peak-to-peak amplitude of approximately 0.015 and 0.01V for still water and still air, respectively. These fluctuations on the signal are very small and almost insignificant when compared to voltage readings observed when PVDF is exposed to cavitation flow. As seen in Figure 43, the raw signal of the PVDF for still water condition is

consistent for sampling length of 15 ms. Other from these small fluctuations, there were no strange fluxes and irregularities observed on the signals. Thus, it is safe to conclude that all the signals obtained here in this work for PVDF subjected to cavitation are accurate and no unwanted factors such as grounding issues are affecting the overall signal.

4.5 PVDF and Hydrophone Signals from Far Field

Following the collapse of the cavitation bubbles are shock waves that can be recognized far away from the site of cavitation. In order to identify this, PVDF film and hydrophone sensors were placed close to one side of the water container, while the horn was situated close to the opposite side. The raw data for from PVDF with one layer of tape subjected at 75% vibrating amplitude is seen on Figure 46.

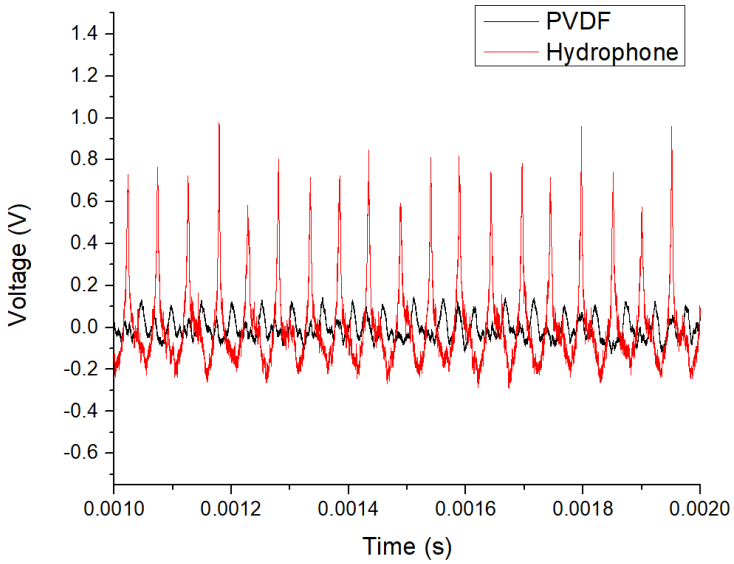

Figure 46. Raw signals obtained from sensors located at far field when horn is vibrating at 75% amplitude

The data taken show that the hydrophone records higher voltage readings than the PVDF film. Thus, the hydrophone performs to be a more sensitive sensor compared to PVDF film in

quantifying pressures emitted by shock waves. The cumulative peak rate of the hydrophone is graphed in Figure 47.

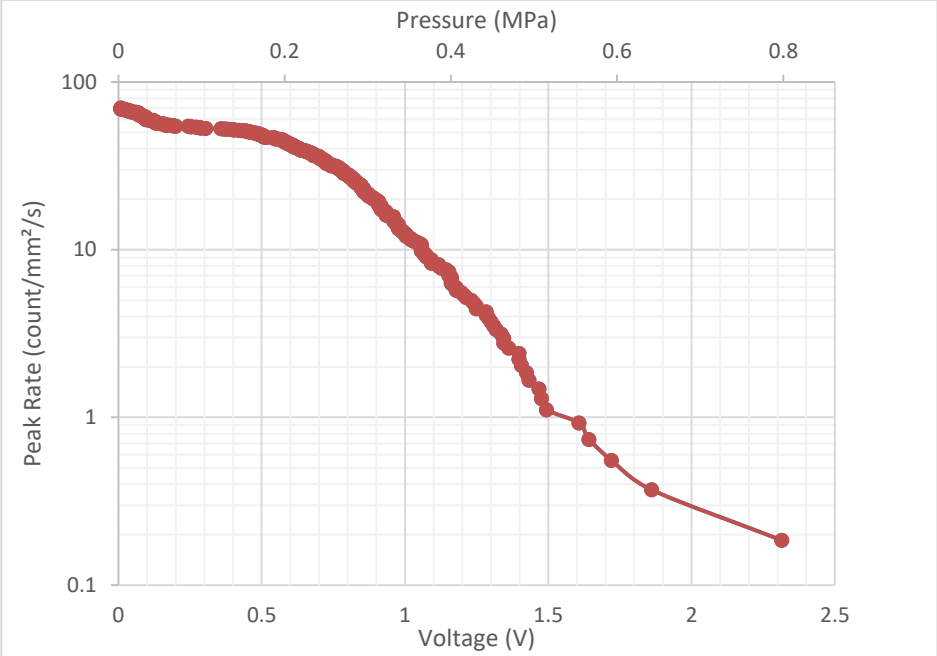

Figure 47. Cumulative peak rate as a function of voltage as recorded by hydrophone sensor

The trend of the cumulative peak rate obtained from hydrophone displays similarity with the cumulative peak rates obtained when measuring direct impacts of bubble collapses using the PVDF sensor. It also shows a non-linear curve for values of pressure (or voltage) close to zero and a linear part thereafter. This implies that the bubble collapse impacts detected by PVDF sensor emit a corresponding intensity of shock wave which also follows an exponential law relationship between peak rate and pressure.

4.6 Calibration

Signals obtained during the calibration of the PVDF sensor are presented in Figure 48. It shows trial runs when a ball weight of 1.487g is dropped from a height of 400mm. This was conducted before and after subjecting the film to cavitation experimental runs. The graph demonstrates good repeatability between these runs.

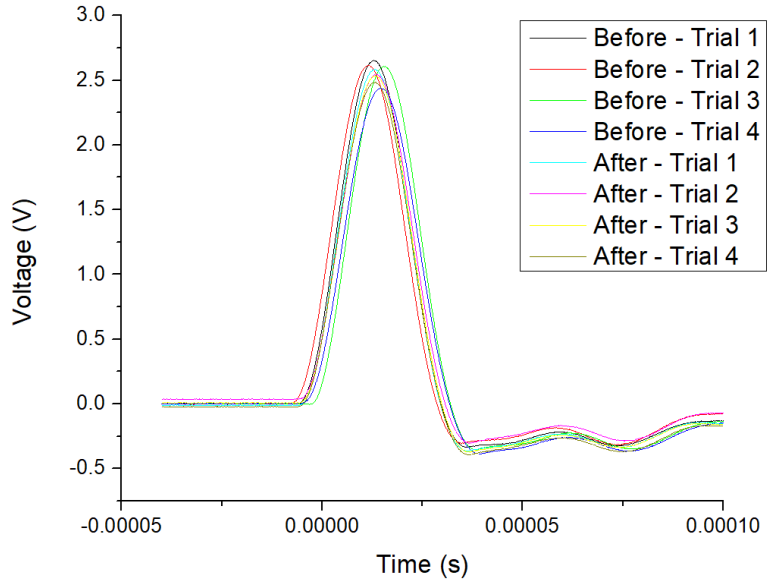

Figure 48. Signal when 1.487g of ball was dropped into the PVDF film from a height of 400mm

Figure 49 shows the full calibration curve obtained after doing several drop test for balls with different weights. The sensor sensitivity is the slope of the linear fit curve. In this case, the sensitivity value is 6 mV/N and is observed to be consistent before and after the cavitation experiment. The R^2 value for the fitted line is 0.9944 and 0.9974 for the before and after condition, respectively, which are almost equal to 1. This proves excellent linear relationship between impact force and the induced voltage produced by the PVDF sensor. The data shows good reproducibility of calibration curve before and after the experiment which ascertains that the sensor remained in good condition all throughout the experimental runs. The full data of the calibration curve is detailed in the Appendix.

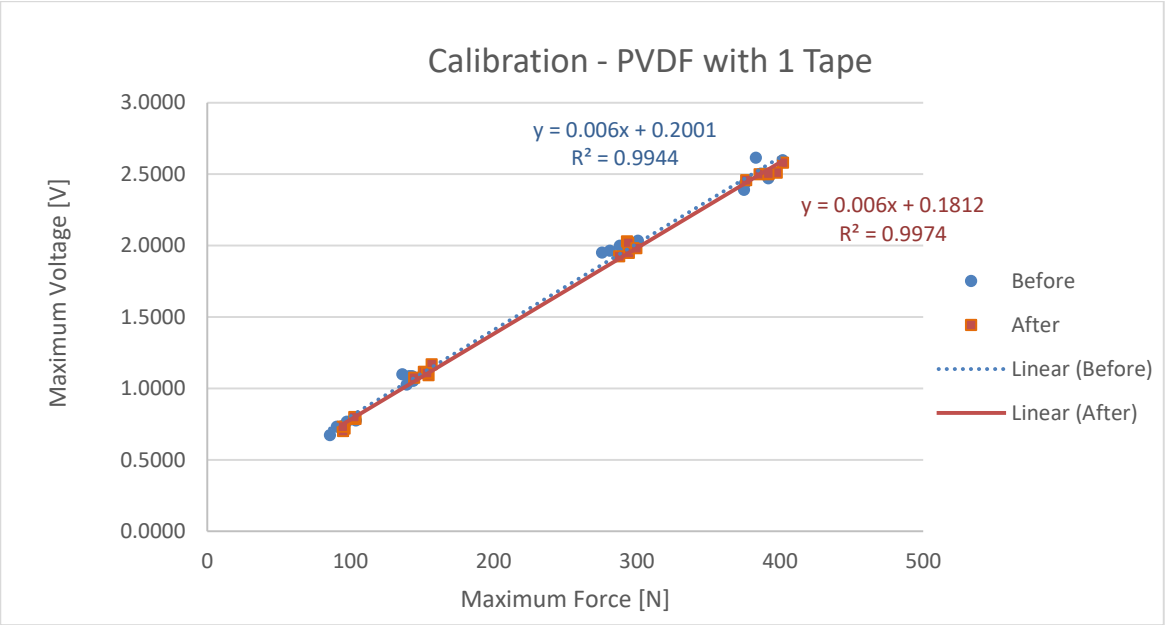

Figure 49. Calibration curve for the PVDF film with one layer of protective tape

The calibration curve is proven linear from 0.75V to 2.5V. Within this range, the calibration factor which is 6 mV/N holds true. Although the conducted experimental runs for different vibration amplitude reaches to approximately 3.2 V as seen in Figure 36, this small difference from 2.5V is not highly significant and that the linearity of the calibration curve will still be valid up to this point.

4.7 Comparison with Pitting Test

Aidoo [27] has conducted pitting test on aluminum alloy (EN AW-7075 T6511) having yield strength of 521 MPa. His experiments were carried out on the same experimental setup utilized in this study. However, his study was focused on analyzing pits generated on the material which was subjected to 100% amplitude regime (which is equivalent to 57 µm vibration amplitude) and exposing it to varying time duration of 40 s, 60 s and 80 s. Figure 50 shows his acquired data of the cumulative impact count per surface area whose pit diameter is larger than the corresponding pit diameter value on the horizontal axis.

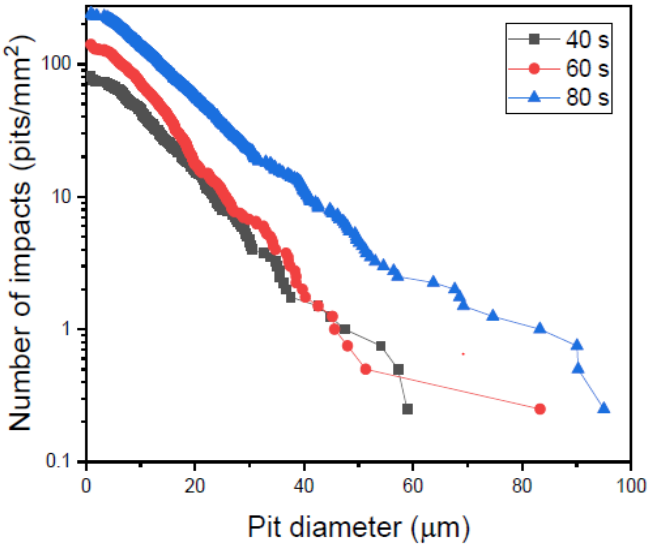

Figure 50. Cumulative number of impacts vs. pit diameter as obtained by Aidoo [27]

To compare the number of impacts to the peak rate utilizing the 100% vibration amplitude condition, the vertical axis is converted to give pit rate which is the number of pits formed in a unit area per unit time. Also, an appropriate load threshold value must be applied to the peak rate data. This threshold value is needed to set the minimum force which causes pits on the material's surface. In a study by Bai et. al.[32], they identified that a threshold value of 8.6 N which was based on the impact load that just damages an aluminum foil will most likely not to create damage to other metal materials. Moreover, Okada et. al.[47] found that a 9.1 N impact load is necessary to create a pit of 4 µm in diameter in aluminum. Therefore, a threshold of 8.6 N can be an

acceptable value. The collated post-processed pit rate and peak rate are shown in Figure 51. Notice that the pit rate distribution curve did not significantly change after applying the threshold value.

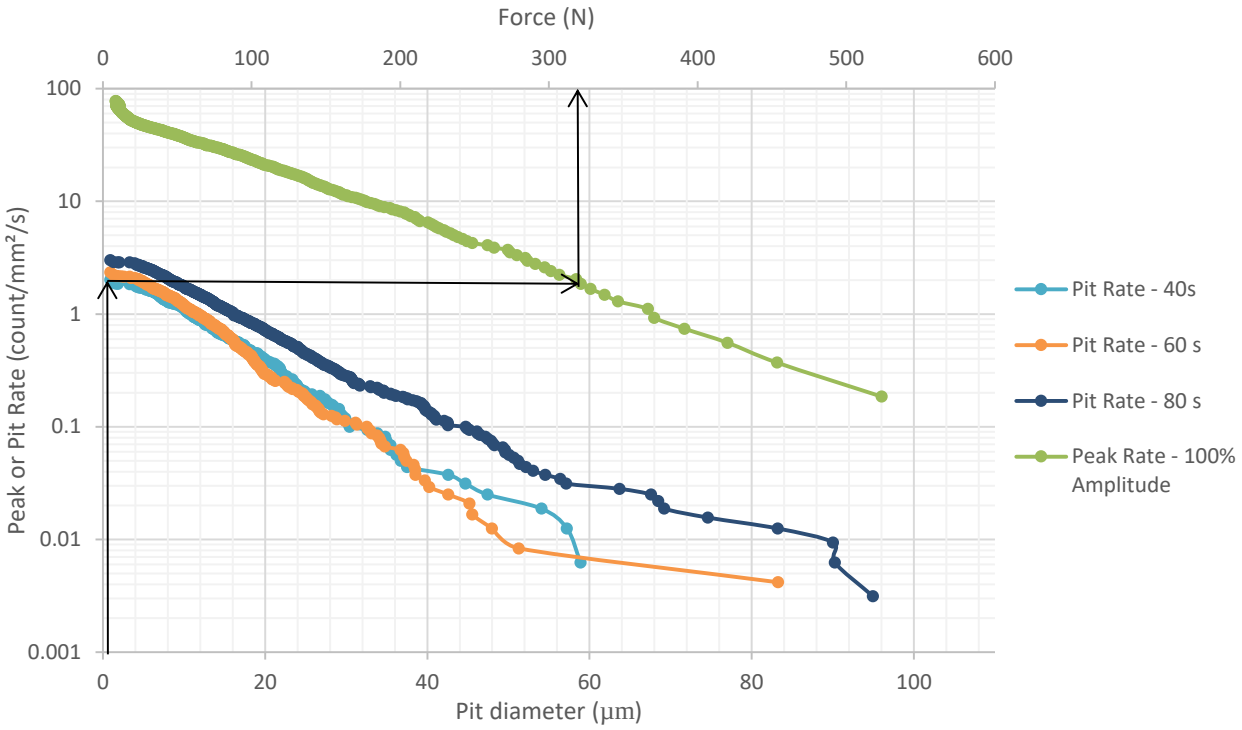

Figure 51. Comparison of distribution of cumulative pit rate and peak rate histograms

Based from Figure 51, the peak rate reaches a maximum value of approximately 80 impacts/mm^2/s while the pit rate is rated maximum at around 3 pits/mm^2/s only. It is clear that there is a remarkable difference between the order of magnitude of the pit rate and impact peak rate. This could imply that not all the bubble collapse impacts proceed to the formation of erosion pits. This is supported by researchers such as Knapp who found out that only one of 3000 cavities cause damage and Robinson and Hammit who identified that only one in 10^4 of the bubble collapses create pits [47]. The impacts that did not generate pits can be weak loads that impart stress only within the elastic region of the material and not reaching its material tensile strength. This means that these weak impact loads cannot create permanent damage but only cause elastic deformation which cannot be detected as pits.

It was proven by Knapp and Stinebring that damage produced during the incubation period is from a single cavitation bubble collapse [47]. Hence, if an individual pit is assumed to be formed from a single impact, then the load needed to create then a pit can be derived by matching the peak rate value with the pitting rate formed during the incubation period. In this case, the pits detected in the sample exposed to 40 s during the pitting test is most likely to have occurred at the incubation period. If the smallest pit in this data, which is 0.9 μm, is taken and its corresponding pit rate is matched with the equivalent peak rate, then a value of 319 N impact load is obtained (see arrows in Figure 51). This is the critical load which marks the onset of pit formation.

5 CONCLUSION

In summary, this thesis study reviewed the research works pertaining to the investigation of the cavitation aggressiveness (Sections 2.7 to 2.8). Based on this, an experimental setup was defined and prepared (Section 3). The cavitation bubbles studied here were generated through the ultrasonic vibratory equipment which was chosen because of its favorable advantages (Section 2.8.1). In the aim to characterize the cavitation impacts generated from acoustic waves produced by ultrasonic horn, the flow of the study is designed to first optimize the methodology before conducting the cavitation aggressiveness test. This was carried out by using PVDF sensor. It was found out that signals obtained from the PVDF sensor are consistent and that a minimum of 3 sample runs will be enough to get a representative cavitation impact data for the set regime. Four different PVDF configurations were prepared and exposed to cavitation. All data gathered from the PVDF film regardless of how it was prepared showed to exhibit an exponential relationship between the cumulative peak rate and peak amplitude. Among the four PVDF configurations examined, the PVDF film with added one layer of protective tape is deemed to be the best suitable film configuration to be used wherein a balance between sensitivity and durability of the sensor to cavitation erosion were considered. Cavitation aggressiveness test was done on this selected film configuration by subjecting it to different vibration amplitude. Results showed that increasing the amplitude leads to intense impacts generating higher maximum peak voltage. FFT was applied on the PVDF signals and it revealed that impacts mostly occur at the frequency equivalent to frequency of the horn. However, it was also observed that there are dominantly high peak impacts which occur after some cycles of horn vibration. These prominent peaks denote presence of large cluster of cavity that collapses at its own collapse frequency that is lower than the frequency of the horn. It was also observed that the frequency of these high intensity collapses decreases with increasing vibration amplitude. When the peak rate was compared to the pitting rate, it showed that there is a significantly high difference between the pitting rate and peak rate in terms of the order of magnitude, the peak rate being higher. This could mean that not all impacts cause damage to the material surface. Moreover, if it assumed that during the incubation period, each pit is caused by a high impact force, then a load of 319 N is necessary to create a 0.9 μm diameter pit on aluminum alloy.

6 REFERENCES

[1] Y. F. Ronald, *Cavitation*. London: Imperial College Press, 1999.

[2] S. C. Roy, "Modeling and analysis of material behavior during cavitation erosion," *Mater. Univ. Grenoble Alpes*, 2015.

[3] K.-H. Kim, C. Georges, J.-P. Franc, and A. Karimi, *Advanced Experimental and Numerical Techniques for Cavitation Erosion Prediction*, vol. 106. Dordrecht: Springer Science+Business Media, 2014.

[4] J.-M. Franc, Jean-Pierre; Michel, *Fundamentals of Cavitation*. Dordrecht: Kluwer Academic Publishers, 2004.

[5] I. Tzanakis, D. G. Eskin, A. Georgoulas, and D. K. Fytanidis, "Incubation pit analysis and calculation of the hydrodynamic impact pressure from the implosion of an acoustic cavitation bubble," *Ultrason. Sonochem.*, vol. 21, no. 2, pp. 866–878, 2014.

[6] F. J. Fuchs, *Ultrasonic cleaning and washing of surfaces*. Elsevier Ltd., 2014.

[7] X. Ding, Y. Kang, D. Li, X. Wang, and D. Zeng, "Experimental investigation on surface quality processed by self-excited oscillation pulsed waterjet peening," *Materials (Basel).*, vol. 10, no. 9, 2017.

[8] D. Odhiambo and H. Soyama, "Cavitation shotless peening for improvement of fatigue strength of carbonized steel," *Int. J. Fatigue*, vol. 25, no. 9–11, pp. 1217–1222, 2003.

[9] Y. Gao, B. Wu, Z. Liu, Y. Zhou, N. Shen, and H. Ding, "Ultrasonic Cavitation Peening of Stainless Steel and Nickel Alloy," *J. Manuf. Sci. Eng.*, vol. 136, no. 1, p. 014502, 2013.

[10] C. E. Brennen, "Cavitation in medicine.," *Interface Focus*, vol. 5, no. 5, p. 20150022, 2015.

[11] Y. Tao, J. Cai, X. Huai, B. Liu, and Z. Guo, "Application of Hydrodynamic Cavitation to Wastewater Treatment," *Chem. Eng. Technol.*, vol. 39, no. 8, pp. 1363–1376, 2016.

[12] P. Thanekar, P. Gogate, P. Thanekar, and P. Gogate, "Application of Hydrodynamic

Cavitation Reactors for Treatment of Wastewater Containing Organic Pollutants: Intensification Using Hybrid Approaches," *Fluids 2018, Vol. 3, Page 98*, vol. 3, no. 4, p. 98, 2018.

[13] S. Sutariya, V. Sunkesula, R. Kumar, and K. Shah, "Emerging applications of ultrasonication and cavitation in dairy industry: a review," *Cogent Food Agric.*, vol. 4, no. 1, pp. 1–21, 2018.

[14] L. Shengcai, *Cavitation of Hydraulic Machinery*. London: Imperial College Press, 2000.

[15] J. Blake, "Cavitation Bubbles Near Boundaries," *Annu. Rev. Fluid Mech.*, vol. 19, no. 1, pp. 99–123, 1987.

[16] C. E. Brennen, *Cavitation and Bubble Dynamics*. New York: Oxford University Press, 1995.

[17] B. K. Sreedhar, S. K. Albert, and A. B. Pandit, "Cavitation damage: Theory and measurements – A review," *Wear*, vol. 372–373, pp. 177–196, 2017.

[18] Y. Kurosawa *et al.*, "Basic study of brain injury mechanism caused by cavitation," *Proc. 31st Annu. Int. Conf. IEEE Eng. Med. Biol. Soc. Eng. Futur. Biomed. EMBC 2009*, pp. 7224–7227, 2009.

[19] H. S. Lee, S. W. Hwang, and K. Yamamoto, "Examination of cavitation-induced surface erosion pitting of a mechanical heart valve using a solenoid-actuated apparatus," *KSME Int. J.*, vol. 17, no. 9, pp. 1339–1348, 2003.

[20] M. Muller, *Dynamic behavior of cavitation bubbles generated by laser*. Liberec: Technical University of Liberec, 2008.

[21] J. P. Franc, "The rayleigh-plesset equation: A simple and powerful tool to understand various aspects of cavitation," *CISM Int. Cent. Mech. Sci. Courses Lect.*, vol. 496, pp. 1–41, 2007.

[22] J. K. Choi and G. L. Chahine, "Relationship between material pitting and cavitation field impulsive pressures," *Wear*, vol. 352–353, pp. 42–53, 2016.

[23] R. P. Tong, W. P. Schiffers, S. J. Shaw, J. R. Blake, and D. C. Emmony, “The role of ‘splashing’ in the collapse of a laser-generated cavity near a rigid boundary,” *J. Fluid Mech.*, vol. 380, pp. 339–361, 1999.

[24] D. Heath, B. Širok, M. Hočevar, and B. Pečnik, “The Use of the Cavitation Effect in the Mitigation of CaCO3 Deposits,” *J. Mech. Eng.*, vol. 59, pp. 203–215, 2013.

[25] K. Kotian, “Detection of in-plane stress waves with Polyvinylidene Fluoride (PVDF) sensors,” The Ohio State University, 2013.

[26] J. P. Franc, M. Riondet, A. Karimi, and G. L. Chahine, “Material and velocity effects on cavitation erosion pitting,” *Wear*, vol. 274–275, pp. 248–259, 2012.

[27] E. O. Aidoo, “Material response on the cavitation bubble collapses,” Technical University of Liberec, 2018.

[28] N. Berchiche, J. P. Franc, and J. M. Michel, “A Cavitation Erosion Model for Ductile Materials,” *J. Fluids Eng.*, vol. 124, no. 3, p. 601, 2002.

[29] D. Carnelli, A. Karimi, and J. P. Franc, “Evaluation of the hydrodynamic pressure of cavitation impacts from stress-strain analysis and geometry of individual pits,” *Wear*, vol. 289, pp. 104–111, 2012.

[30] S. Singh, J.-K. Choi, and G. L. Chahine, “Characterization of Cavitation Fields From Measured Pressure Signals of Cavitating Jets and Ultrasonic Horns,” *J. Fluids Eng.*, vol. 135, no. 9, p. 091302, 2013.

[31] J. Hujer, J. Carrat, M. Müller, and M. Riondet, “Impact load measurements with a PVDF pressure sensor in an erosive cavitating flow,” *J. Phys. Conf. Ser.*, vol. 656, no. 1, pp. 1–5, 2015.

[32] F. Bai, K. A. Saalbach, L. Wang, and J. Twiefel, “Investigation of impact loads caused by ultrasonic cavitation bubbles in small gaps,” *IEEE Access*, vol. 6, no. December, pp. 64622–64629, 2018.

[33] Y. C. Wang and Y. W. Chen, “Application of piezoelectric PVDF film to the measurement

of impulsive forces generated by cavitation bubble collapse near a solid boundary," *Exp. Therm. Fluid Sci.*, vol. 32, no. 2, pp. 403–414, 2007.

[34] J.-P. Franc, M. Riondet, A. Karimi, and G. L. Chahine, "Impact Load Measurements in an Erosive Cavitating Flow," *J. Fluids Eng.*, vol. 133, no. 12, p. 121301, 2011.

[35] M. S. Vohra, N. A. Prasanth, W. L. Tan, and S. H. Yeo, "Analysis of Impact Load Induced by Ultrasonic Cavitation Bubble Collapse Using Thin Film Pressure Sensors," vol. 11, no. 11, pp. 1810–1815, 2017.

[36] I. Tzanakis, L. Bolzoni, D. G. Eskin, and M. Hadfield, "Evaluation of Cavitation Erosion Behavior of Commercial Steel Grades Used in the Design of Fluid Machinery," *Metall. Mater. Trans. A Phys. Metall. Mater. Sci.*, vol. 48, no. 5, pp. 2193–2206, 2017.

[37] H. Liu, T. Zhang, and C. Kang, "Evaluation of cavitation erosion resistance of copper alloy in different liquid media," *Mater. Corros.*, vol. 69, no. 7, pp. 917–925, 2018.

[38] A. Pola, L. Montesano, M. Tocci, and G. M. La Vecchia, "Influence of ultrasound treatment on cavitation erosion resistance of AlSi7 alloy," *Materials (Basel).*, vol. 10, no. 3, 2017.

[39] S. Paepenmöller, J. Kuhlmann, M. Blume, and R. Skoda, "Assessment of flow aggressiveness at an ultrasonic horn cavitation erosion test device by PVDF pressure measurements and 3D flow simulations," in *Proceedings of the 10th International Symposium on Cavitation*, 2018.

[40] A. K. Krella and D. E. Zakrzewska, "Cavitation Erosion – Phenomenon and Test Rigs," *Adv. Mater. Sci.*, vol. 18, no. 2, pp. 15–26, Jun. 2018.

[41] Y. C. Lee, J. M. Yu, and S. W. Huang, "Fabrication and Characterization of a PVDF Hydrophone Array Transducer," *Key Eng. Mater.*, vol. 270–273, pp. 1406–1413, 2009.

[42] M. Müller, J. Hujer, M. Kotek, and P. Zima, "Identification of collapse patterns of cavitation bubbles close to a solid wall," *EPJ Web Conf.*, vol. 45, p. 01120, 2013.

[43] A. Žnidarčič, R. Mettin, C. Cairós, and M. Dular, "Attached cavitation at a small diameter ultrasonic horn tip," *Phys. Fluids*, vol. 26, no. 2, pp. 0–17, 2014.

[44] J. Hujer and M. Müller, “Calibration of PVDF Film Transducers for the Cavitation Impact Measurement,” *EPJ Web Conf.*, vol. 180, p. 02036, 2018.

[45] J. Katz, M. Ylönen, P. Saarenrinne, J. Miettinen, J.-P. Franc, and M. Fivel, “Cavitation Bubble Collapse Monitoring by Acoustic Emission in Laboratory Testing,” *Proc. 10th Int. Symp. Cavitation*, 2019.

[46] P. R. Birkin, D. G. Offin, C. J. B. Vian, and T. G. Leighton, “Multiple observations of cavitation cluster dynamics close to an ultrasonic horn tip,” *J. Acoust. Soc. Am.*, vol. 130, no. 5, pp. 3379–3388, 2011.

[47] T. Okada, Y. Iwai, and K. Awazu, “A study of cavitation bubble collapse pressures and erosion part 1: A method for measurement of collapse pressures,” *Wear*, vol. 133, no. 2, pp. 219–232, 1989.

APPENDIX

Calibration Data

Table 3. Calibration before exposing the PVDF to cavitation impact experimental runs

Trial	Mass of ball (g)	h_1 (mm)	h_2 (mm)	v_1 (m/s)	v_2 (m/s)	t_1 (us)	t_2 (us)	τ (µs)	F_{max} (N)	U_{max} (V)
1.1	1.487	400	185	2.80	1.90	33.98	69.67	35.69	391.96	2.47
1.2	1.487	400	183	2.80	1.89	32.35	68.79	36.43	383.13	2.62
1.3	1.487	400	182	2.80	1.89	37.43	72.11	34.69	401.98	2.60
1.4	1.487	400	167	2.80	1.81	35.29	71.78	36.49	375.62	2.43
1.5	1.487	400	168	2.80	1.81	34.45	71.05	36.60	374.91	2.39
1.6	1.487	400	166	2.80	1.80	36.15	71.55	35.40	386.77	2.50
2.1	1.043	400	172	2.80	1.83	32.17	66.55	34.38	281.28	1.96
2.2	1.043	400	181	2.80	1.88	33.87	67.78	33.91	288.09	2.00
2.3	1.043	400	192	2.80	1.94	31.23	65.05	33.82	292.35	2.01
2.4	1.043	400	176	2.80	1.86	30.61	65.85	35.24	275.68	1.95
2.5	1.043	400	190	2.80	1.93	33.11	65.91	32.79	300.85	2.03
3.1	0.440	400	195	2.80	1.95	35.50	64.73	29.23	143.14	1.09
3.2	0.440	400	202	2.80	1.99	31.55	62.48	30.93	136.27	1.10
3.3	0.440	400	200	2.80	1.98	35.93	65.17	29.25	143.83	1.05
3.4	0.440	400	199	2.80	1.97	32.07	61.87	29.80	141.00	1.09
3.5	0.440	400	196	2.80	1.96	32.60	62.68	30.08	139.27	1.03
4.1	0.253	400	205	2.80	2.00	35.03	60.97	25.93	93.74	0.73
4.2	0.253	400	201	2.80	1.98	36.13	59.44	23.31	103.87	0.77
4.3	0.253	400	216	2.80	2.06	35.75	62.92	27.17	90.47	0.73
4.4	0.253	400	219	2.80	2.07	34.97	60.25	25.28	97.50	0.77
4.5	0.253	400	195	2.80	1.95	28.27	56.34	28.07	85.70	0.67

Table 4. Calibration after exposing the PVDF to cavitation impact experimental runs

Trial	Mass of ball (g)	h_1 (mm)	h_2 (mm)	v_1 (m/s)	v_2 (m/s)	t_1 (us)	t_2 (us)	τ (µs)	F_{max} (N)	U_{max} (V)
1.1	1.487	400	178	2.80	1.87	35.08	69.61	34.52	402.08	2.58
1.2	1.487	400	174	2.80	1.85	35.03	70.29	35.26	391.90	2.50
1.3	1.487	400	171	2.80	1.83	35.05	69.67	34.62	397.75	2.51
1.4	1.487	400	160	2.80	1.77	34.48	69.70	35.22	385.88	2.50
1.5	1.487	400	161	2.80	1.77	34.66	70.81	36.15	376.41	2.46
2.1	1.043	400	187	2.80	1.91	34.16	67.70	33.54	293.20	2.03
2.2	1.043	400	177	2.80	1.86	34.83	67.92	33.08	293.97	2.02
2.3	1.043	400	194	2.80	1.95	34.50	68.15	33.65	294.47	1.95
2.4	1.043	400	186	2.80	1.91	34.82	67.59	32.77	299.74	1.98
2.5	1.043	400	177	2.80	1.86	34.02	67.81	33.80	287.75	1.92
3.1	0.440	400	204	2.80	2.00	33.81	61.12	27.31	154.64	1.09
3.2	0.440	400	224	2.80	2.09	33.29	61.75	28.46	151.39	1.11
3.3	0.440	400	214	2.80	2.05	33.63	60.86	27.23	156.69	1.17
3.4	0.440	400	207	2.80	2.01	33.47	61.07	27.60	153.50	1.11
3.5	0.440	400	213	2.80	2.04	32.62	62.09	29.46	144.65	1.07
4.1	0.253	400	228	2.80	2.11	31.60	57.53	25.93	95.90	0.72
4.2	0.253	400	229	2.80	2.12	33.16	57.19	24.03	103.57	0.78
4.3	0.253	400	215	2.80	2.05	31.93	57.80	25.86	94.94	0.70
4.4	0.253	400	229	2.80	2.12	32.64	56.89	24.25	102.64	0.80
4.5	0.253	400	220	2.80	2.08	31.52	57.58	26.06	94.71	0.73